Generated using the official AMS LaTeX template v6.1

Observed variability in convective cell characteristics and near-storm environments across the sea and bay-breeze fronts in southeast Texas

Milind Sharma[a] , Anita D. Rapp[a] , Christopher J. Nowotarski[a] , and Sarah D. Brooks[a]

[a] *Department of Atmospheric Sciences, Texas A&M University, College Station, Texas, USA*

Corresponding author: Milind Sharma, milindsharma@tamu.edu

ABSTRACT: During the DOE ARM TRACER IOP spanning June to September 2022, two fixed ARM sites and a mobile team concurrently sampled the air mass heterogeneity across sea and bay-breeze fronts around the greater Houston metropolitan region. Here, we quantify the spatiotemporal variability between maritime (coastal/bay side of breeze fronts) and continental (inland side of breeze fronts) air masses over 15 IOP days characterized by strong sea breeze forcing. We analyze environmental profile data from 177 radiosondes and use S- and C-band radar data to track and quantify the variability in attributes of more than 2300 shallow and transitioning cells across different air masses. Composite analysis of environmental profiles indicates that during early afternoon, the sea-breeze maritime air mass exhibits lower CAPE than the bay-breeze maritime air mass. As the sea breeze advances inland with time, CAPE within the maritime air mass exceeds that of the continental air mass to the north of the breeze fronts. In general, maritime cells have larger mean composite reflectivity and cell widths compared to continental cells; however, the response varies between shallow and transitioning cells. Mean composite 20-dBZ echo-top heights, however, are similar across air masses for both shallow and transitioning cells. The continental and maritime inflow air mass for transitioning cells has significantly different mean values for mixed-layer entrainment CAPE, lifted condensation level, level of free condensation, boundary layer depth, and diluted equilibrium level. For shallow cells, only total precipitable water shows a significant difference.

SIGNIFICANCE STATEMENT: The greater Houston metropolitan area is a natural laboratory for understanding the individual impacts of background meteorology and aerosols on convective clouds. Due to its proximity to the Gulf coast and Galveston Bay, the Houston region experiences a diurnal precipitation cycle in the summer, driven by convection triggered from sea and bay-breeze fronts. These fronts act as a boundary between air masses with distinct thermodynamic and environmental characteristics. Convergence along these fronts, and interactions between storm outflow and the fronts, facilitate convection initiation in different mesoscale air masses. This study quantifies the heterogeneity among these air masses while investigating their influence on cloud microphysics. We find that the effect of air mass heterogeneity is more pronounced for the bulk microphysical properties in shallow clouds.

1. Introduction and background

Deep moist convection is a pivotal component of the global climate system, facilitating the vertical redistribution of moisture, heat, momentum, and pollutants. However, the ingredients responsible for triggering deep moist convection initiation or "shallow-to-deep" transition are still less clear (Derbyshire et al. 2004; Khairoutdinov and Randall 2006; Waite and Khouider 2010; Zhang and Klein 2010; Genio et al. 2012; Hohenegger and Stevens 2013; Nelson et al. 2022; Morrison et al. 2022; Giangrande et al. 2023; Marquis et al. 2023). One of the primary reasons for this knowledge gap is the lack of sufficient observations at the spatiotemporal scales needed to capture the growth of deep convective clouds or mesoscale variability in their environments. Additionally, the current numerical models fail to resolve convective scale processes at both coarse and fine spatiotemporal scales (Bryan et al. 2003). Thanks to the recent Atmospheric Radiation Measurement (ARM) research field campaigns (Jensen et al. 2016; Martin et al. 2017; Fast et al. 2019; Varble et al. 2021; Jensen et al. 2022), there has been a significant advancement in our understanding of cloud-scale processes and their evolution in response to initial thermodynamical and dynamical conditions. Nonetheless, the extent to which local environmental heterogeneity controls the fate of a developing convective cloud is still debatable (Romps and Kuang 2010; Böing et al. 2012; Dawe and Austin 2012; Brast et al. 2016; Rousseau-Rizzi et al. 2017; Kurowski et al. 2019; Tian et al. 2021; Morrison et al. 2022).

Another reason for an incomplete understanding of the evolution of a convective cloud is its dependency on complex thermodynamic and dynamical interactions between convection and the environment across a wide range of spatiotemporal scales (Johnson et al. 1999; Martin and Xue 2006; Zhang and Klein 2010; Kirshbaum 2011; Hohenegger and Stevens 2013; Rieck et al. 2014; Moser and Lasher-Trapp 2017; Bachmann et al. 2020; Henkes et al. 2021; Chen et al. 2023). These interactions can become more intricate in the presence of environmental and land-surface heterogeneity, forcing mesoscale circulations, such as the sea and bay-breeze fronts (collectively referred to as SBF; Weaver 2004). The diurnal precipitation cycle associated with thermally direct circulations in coastal regions, like the ubiquitous summertime SBF in southeast Texas, is greatly influenced by mesoscale gradients in surface fluxes, alongside modifications to lower-tropospheric instability and moisture induced by the SBF (Ohashi and Kida 2002).

The phase and intensity of the diurnal precipitation cycle over land is known to be closely tied to the evolution of planetary boundary layer processes (hereinafter referred to as PBL; Schlemmer et al. 2012; Harvey et al. 2022). All else being equal, the horizontal scale of mesoscale thermal forcing coupled with PBL processes governs the cumulus cloud width, updraft buoyancy, and vertical velocity (Grabowski et al. 2006; Robinson et al. 2008; Morrison et al. 2022). The initial updraft width at the cloud base largely determines which thermals in a cloud field will undergo the deepest ascent and have a longer lifetime (Rousseau-Rizzi et al. 2017; Wilhelm et al. 2023). The size and strength of updrafts at or ahead of the SBF typically scale with the PBL height under constant surface heat fluxes and calm wind conditions, but the scaling breaks down when environmental wind is included (Fu et al. 2022). Similarly, Rieck et al. (2014) found that instead of scaling with the PBL height, evolution of the largest clouds involved a complex interplay between the characteristics of triggered mesoscale circulations and the diurnal cycle of surface heating. Once deep convection initiates, other mesoscale processes such as gravity waves and cold pools also play a role in the onset and propagation of deep convection (Khairoutdinov and Randall 2006; Schlemmer and Hohenegger 2014; Bechtold et al. 2014; Colin et al. 2019).

The timing and strength of mesoscale convergence along SBFs and/or during collision of a SBF and a convective outflow boundary can also influence the evolution of cloud width and depth (Rieck et al. 2014; Birch et al. 2015; Rousseau-Rizzi et al. 2017; Fu et al. 2022). In their idealized simulations of convection initiation (hereinafter referred to as CI) along SBF convergence boundaries, Fu et al. (2021) found three generations of deep convection. While the first two generations occurred along the SBF convergence line, the third generation of convection developed from the intersection of the cold pools produced by the second generation of convection through collision between the gust front and the SBF. Constructive and destructive interactions between SBF and local thermal circulations such as coupling with internal gravity waves, horizontal convective rolls and urban heat island circulations can also initiate deep convection with updrafts of varying intensity (Nicholls et al. 1991; Wakimoto and Atkins 1994; Ohashi and Kida 2002; Fovell 2005; Cheng and Byun 2008; Dandou et al. 2009). The strength of mesoscale convergence along the SBF can significantly vary based on changes in land-surface sensible heat flux, convective turbulence, and the strength of synoptic onshore/offshore flow. As buoyant production of PBL turbulence increases during peak daytime heating, it leads to frontolysis of SBF and slowing of inland penetration speed by weakening the thermal gradient, thereby controlling the thermal and dynamical forcing for deep convection.

Background meteorological variability and anthropogenic aerosol perturbations in the greater Houston metropolitan area offer opportunistic experiments to study the life cycle of isolated convection (Fridlind et al. 2019). Owing to the differential heating between land and water (Gulf of Mexico to the south and Galveston Bay to the east), and a considerable heterogeneity in land use land cover, the greater Houston area undergoes a relatively rapid evolution of the diurnal PBL and mesoscale convergence zone along the SBF as it advances north. Typically, there are several mesoscale air masses present in the Houston region on a convective day (continental air, maritime Gulf-of-Mexico air, maritime Galveston Bay air, and convective outflow). Each air mass carries unique thermodynamic characteristics, capable of influencing the development of nearby convective cells if it serves as storm inflow. Therefore, it is essential to measure the thermodynamic variability across these air masses, emphasizing the need for adaptable mobile measurements. Aerosol-convection interactions are yet another factor that can introduce nonlinear changes in the microphysical and dynamical structure of clouds, thus contributing to uncertainty in cloud radiative forcing in the global climate system (Khain et al. 2005; Li et al. 2011; Morrison and Grabowski 2011; Grabowski 2015; Thornton et al. 2017; Lebo 2018; Heikenfeld et al. 2019; Marinescu et al. 2021). As a result, it can be challenging to quantify the causal effect of meteorological variability and aerosols independently. With this goal in mind, the mobile measurement team from Texas A&M

University (TAMU) joined forces with the Tracking Aerosol-Convection Interaction Experiment (TRACER) field campaign, supported by the U.S. Department of Energy's (DOE) ARM facility. However, in this paper, we focus on determining the potential effects of meteorological variability on convection, so that subsequent work can isolate any aerosol-dependent effects within the proper meteorological context.

The strength of subcloud ascent induced by mesoscale thermodynamic forcing predominantly dictates the initial width and vertical acceleration of updraft parcels as they encounter entrainment-driven dilution, adverse vertical perturbation pressure gradients, and synoptic-scale downdrafts (Peters et al. 2020; Morrison et al. 2022). The TAMU TRACER field campaign sought to sample the air masses that were unsampled by the fixed ARM sites. This approach aimed to enhance our understanding of how mesoscale heterogeneity in ambient meteorological conditions and aerosol concentrations affects the evolution of convective clouds around the Houston region. A spatial map of the fixed ARM sites along with the TAMU deployment locations is shown in Fig. 1. The main objective of this study is to characterize the spatiotemporal variability in thermodynamic and kinematic environments and convective cell characteristics across the SBF for 15 TAMU TRACER Intensive Operational Period (IOP) days with a well-defined SBF and predominantly isolated convective cells. These IOPs occurred during July–September 2022, on days when a subtropical high pressure system prevailed over southeastern Texas, supporting inland propagating SBF and isolated to scattered convective cells in a low-shear environment. In the absence of direct measurements of updraft vertical velocity, radar proxies for updraft intensity and width such as maximum composite reflectivity, 20-dBZ echo-top height, and convective cell area can be used to track the evolution of convective updraft life cycle. We investigate whether the observed differences in the aforementioned radar-based cell attributes for shallow and deep convective clouds on either side of the SBF can be explained solely based on the thermodynamic variability. We hypothesize that the deep convective clouds originating in the air mass with larger thermodynamic forcing in the form of larger values of convective available potential energy (CAPE) and free tropospheric environmental humidity will exhibit larger cloud width, composite reflectivity, and radar echo-top heights.

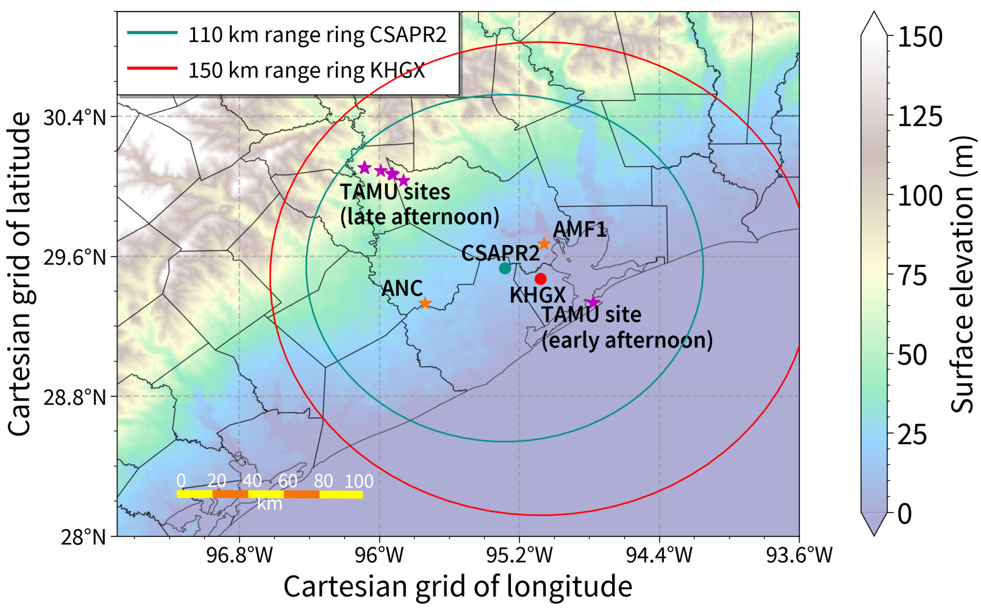

141 Fig. 1. Geographical illustration of the fixed ARM sites (AMF1 and ANC) and the mobile TAMU sites during early and late afternoon deployments. Gray range rings on the map represent the 110 and 150 km range rings for the CSAPR2 and KHGX radars, respectively. Surface elevation is shaded.

2. Data and Methods

a. TAMU TRACER mobile sampling strategy

The 15 TAMU TRACER IOP days analyzed here featured a well-defined SBF that was forecast to trigger isolated convection in and around the Houston metropolitan region on enhanced operation days for the broader TRACER project. The adaptive, fully mobile TAMU onsite radiosonde[1] deployments were targeted to sample the thermodynamic and kinematic profiles of air masses unsampled by the fixed ARM sites via two deployments each day with radiosonde launches simultaneous to those at the ARM sites. For the early afternoon deployment, we launched a radiosonde between 1230 and 1400 LT from Galveston, TX when the sea breeze was typically to the southeast of both ARM sites and the Galveston bay breeze was between them. During the afternoon, the SBF moved inland (sometimes reinforced with storm outflow) and overtook both ARM sites. During this period, the TAMU team would relocate to an inland deployment site to sample the continental air mass north of the SBF, while the ARM sites sampled the maritime air mass. The late afternoon radiosonde launches varied between 1530 and 1830 LT. Both TAMU radiosonde deployments were accompanied by a surface weather station deployment to provide surface observations for each sounding.

b. Upper-air measurements

The ARM sites employed Vaisala RS41 radiosondes, whereas the iMet-4 research radiosondes were used for TAMU operations. The radiosonde temperature and humidity sensors have different performance characteristics, particularly at temperatures lower than -35 °C. To ensure that any potential time lag issues with the iMet-4 humidity sensor would not impact the accuracy of the dewpoint temperature profile, we conducted a thorough comparison of humidity data obtained from both the Vaisala RS41 and iMet-4 radiosondes. We found that iMet-OS II post-processing software sufficiently rectified the raw humidity profile by accounting for the effects of solar radiation, varying dry bias with height, and time lag errors at temperatures below -35 °C. Although the specific correction factors used were proprietary and not openly available, the corrected humidity profile aligned well with the free-tropospheric humidity profile from the Vaisala RS41 radiosondes.

[1]The TAMU team also conducted surface-level and profiling aerosol measurements during each deployment, but this paper focuses on our radiosonde observations.

The ARM sites consistently launched five radiosondes at specific times on TRACER IOP days with enhanced operations: 1230, 1400, 1530, 1700, and 1830 LT. We classified the ARM radiosonde data into early and late afternoon categories, further segmented based on the air mass within which the radiosonde was launched. Additionally, meteorological measurements on the ozonesondes launched as part of the DOE TRACER-Sonde and TRACER-TCEQ-AQ2 field campaigns (Walter et al. 2023) contributed pre-convective environmental profiles around 1000 LT. These profiles were better suited for representing the environmental conditions favorable for CI around 1100 LT, thus augmenting the ARM and TAMU datasets. Upon aggregating all the radiosonde data, each individual sounding was assigned a representative air mass to differentiate among distinct mesoscale air masses sampled by the radiosondes. This classification process relied on various *in situ* and remote sensing observations.

For the TAMU radiosonde data, the first step in classifying air masses involved reviewing the field deployment notes. This information included instantaneous wind speed and direction from the surface weather station, radar and satellite imagery over the Houston region, and an initial subjective assessment of the air mass category at the time of each radiosonde launch. The next step involved verifying the subjective classification through a manual analysis of time series data for surface meteorological variables (i.e., temperature, dewpoint temperature, wind speed, and wind direction) at the radiosonde launch site. The SBF passage was often indicated by a drop in the temperature, an increase in dewpoint temperature, a sudden spike in wind speed, and/or a rapid shift in wind direction—often shifting to south-southeasterly after the SBF passed the site. Given the presence of multiple gust fronts and cold pool boundaries nearby, we manually reviewed satellite and radar animations close to the launch site and time to eliminate the potential of misidentifying a gust front or cold pool as a SBF. A similar classification procedure was followed for ozonesonde and ARM radiosonde data, which included using meteograms generated from the surface weather stations at each ARM site and additional verification with radar and satellite imagery. Details regarding the timing and air mass classification for all soundings are provided in Table 1.

TABLE 1. Launch times and air mass classification for radiosondes launched during the 15 TAMU TRACER IOP days analyzed in this study. The launch times are indicated using specific text font styles to represent different air mass classification: italics for maritime, bold for continental, and asterisk superscript for pure outflow or outflow-modified air mass.

Deployment date	**Launch time (TAMU site 1)**	**Launch time (TAMU site 2)**	**Launch time (AMF1)**	**Launch time (ANC)**	**Launch time (Ozonesonde)**
26 June 2022	*1857* (Galveston)	**2324** (Waller)	**1730**, *1900*, *2031*, *2200*, *2330*	**1729**, **1903**, **2030**, *2200*, *2330*	None
11 July 2022	*1901* (Galveston)	**2327** (Waller)	**1730**, **1900**, *2030*, *2200*, 2330*	**1730**, **1900**, **2030**, *2200*, *2330*	None
13 July 2022	*1730* (Galveston)	**2204** (Waller)	**1730**, *1900*, *2030*, *2200*, *2331*	**1730**, **1900**, 2030*, 2200*, 2330*	**1502**, *2103* (La Porte, UH)
27 July 2022	*1732* (Galveston)	**2123** (Waller)	*1910*, *2059*, *2200*, *2329*	**1746**, *1911*, *2030*, *2200*, *2330*	**1502** (La Porte)
28 July 2022	*1725* (Galveston)	2132* (Waller)	1730*, *1906*, 2057*, *2331*	**1730**, **1900**, **2030**, *2200*, *2330*	**1458** (UH)
29 July 2022	*1725* (Galveston)	**2109** (Waller)	1900*, 2030*, 2200*, 2331*	**1730**, *1900*, 2200*, 2330*	**1500** (La Porte)
7 August 2022	*1721* (Galveston)	**2127** (Hempstead)	*1730*, *1900*, *2030*, *2200*, *2329*	*2030*, *2200*, *2330*	**1457** (La Porte)
8 August 2022	*1724* (Galveston)	**2131** (Hempstead)	*1730*, *1900*, *2030*, *2200*, *2330*	**1730**, *2030*, *2200*, *2330*	**1444** (La Porte)
9 August 2022	*1726* (Galveston)	**2139** (Hempstead)	*1731*, *1900*, *2030*, *2200*, *2329*	1730*, 1900*, 2030*, 2330*	**1500** (La Porte)
26 August 2022	*1726* (Galveston)	**2134** (Prairie View)	1730*, 1924*, 2200*	1730*, 2031*, 2200*, 2330*	**1506**, **1635**, **1938** (La Porte, Galveston Bay, Beach City)
28 August 2022	*1728* (Galveston)	**2119** (Hempstead)	*1730*, *1901*, *2031*, *2200*, *2331*	**1730**, *2030*, *2200*, *2330*	**1500** (La Porte)
31 August 2022	*1729* (Galveston)	No deployment	*1730*, *1902*, *2032*, *2201*, *2330*	**1730**	*1528* (Galveston Bay)
17 September 2022	*1718* (Galveston)	**2059** (Hockley)	*1730*, *1900*, *2030*, *2200*, *2331*	**1730**, *1900*, *2030*, *2200*, *2330*	**1500** (La Porte)
18 September 2022	*1726* (Galveston)	**2126** (Hockley)	*1731*, *1900*, *2030*, *2200*, *2330*	**1730**, **1900**, *2200*, *2330*	**1501** (La Porte)
19 September 2022	*1659* (Galveston)	**2059** (Hempstead)	*1730*, *1900*, *2030*, *2200*, *2329*	**1730**, *1900*, *2030*, *2200*, *2330*	**1458** (La Porte)

c. KHGX cell tracking and classification

To track the life cycle of convective cells throughout the 15 TAMU TRACER IOP days, we used the PyFLEXTRKR Python package (Feng et al. 2022, 2023). First, KHGX PPI reflectivity data were gridded onto a three-dimensional Cartesian grid with a uniform grid spacing of 500 m in the horizontal and vertical dimensions. We limited our cell tracking period between 1100 and 1900 LT for each IOP, aligning with the typical start of the SBF's inland progression. Furthermore, we exclusively tracked cells that remained within a 150-km radius from the KHGX radar to remove cells that were poorly resolved due to beam broadening at longer ranges. PyFLEXTRKR uses a modified version of the Steiner algorithm (Steiner et al. 1995) for cell tracking. This algorithm incorporates a background reflectivity threshold to distinguish the convective cores from the surrounding stratiform rain within each cell. The reflectivity threshold was chosen to distinguish individual cells in scenarios involving multiple cells in close proximity and to ensure the earliest possible detection of isolated cells. After iterative testing, we subjectively selected the algorithm parameters that best met these goals.

Our goals require us to distinguish between cells that remain shallow and those that transition to deep convection in each air mass. Cells with a 0-dBZ echo-top height always less than or equal to 6 km were classified as shallow cells, and those with a 0-dBZ echo-top height that started below 6 km but eventually attained 7.5 km or higher were considered transitioning cells. All other cells were discarded. Subsequent analysis was conducted only on cells (shallow and transitioning[2]) that did not merge or split throughout their life cycle and were tracked through at least two consecutive KHGX volume scans ($\sim$ 12 minutes). This choice retains only well-tracked cells for a comprehensive analysis of their full life cycle. The evolution of the 0-dBZ echo-top height of the shallow and transitioning cells thus identified is illustrated in Fig. 2.

[2]In the subsequent sections of this paper, the terms "transitioning" and "deep" convective cells will be used interchangeably.

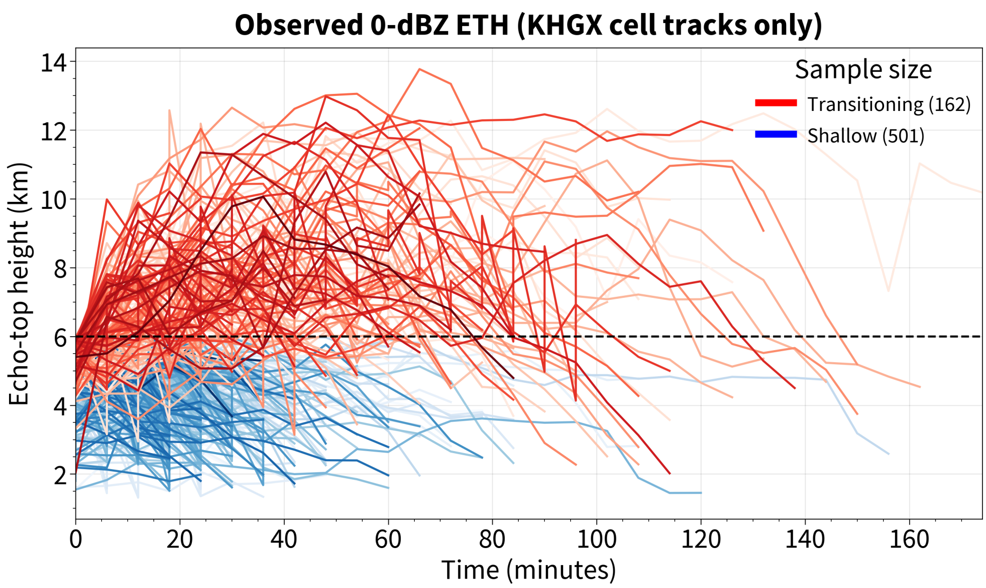

224 FIG. 2. Time series of 0-dBZ echo-top height for shallow (blue) and transitioning (red) convective cells tracked using KHGX gridded reflectivity data. The time series starts at t = 0 minutes, when the tracked cell reaches an area of 10 km^2.

d. Vertical profiles of polarimetric variables from CSAPR2

To capture the rapid evolution of convective clouds (both shallow and transitioning) during the TRACER field campaign, the DOE C-band Scanning ARM Precipitation Radar (CSAPR2) employed an adapted Multisensor Agile Adaptive Sampling strategy (Kollias et al. 2020; Lamer et al. 2023). This sampling strategy was designed to execute a series of RHI scans aimed at "areas of interest" in a target cells. Detailed discussion regarding the CSAPR2 cell tracking strategy during TRACER can be found in Lamer et al. (2023). For this study, we used processed radar variables from CSAPR2 RHI scans including noise-masked reflectivity (Z_H), differential reflectivity (Z_{DR}) corrected for rain attenuation and systematic biases, specific differential phase (K_{DP}), co-polar cross-correlation coefficient, and locations of target cells.

Designated azimuths for CSAPR2 RHI scans corresponded to the maximum values of certain radar variables (see Table 1 in Lamer et al. 2023). Nevertheless, a time gap of around 60 seconds persisted between the timestamp of the PPI scan that provided the target azimuth information and the actual start time of the RHI scan. As a result, the evolving microphysical processes within the storm during this interval could significantly alter the vertical profile of radar variables. To accurately capture the vertical profiles corresponding to the maximum values of Z_H or Z_{DR}, we chose to analyze each RHI scan and select the one with the largest values instead of solely relying on the designated RHI. For K_{DP}, the RHI with the largest vertically integrated K_{DP} value (rather than the absolute maximum value) was chosen. Similar to the KHGX cells, each cell tracked by CSAPR2 was also identified as maritime, continental, or SBF CI and classified as shallow or transitioning. To extract the vertical profile of the radar variables, we began by gridding the RHI data from their native polar coordinate system to a Cartesian grid with a uniform grid spacing of 100 m in both horizontal and vertical dimensions. Each RHI with the largest value of each radar variable was mapped to a track number identified by applying PyFLEXTRKR to CSAPR2 PPI scans. If no target cell was found within 5 km and 2 minutes of an RHI, the RHI was discarded.

e. Sea and bay breeze identification and tracking

Tracking the location of the SBF allowed us to determine the representative air mass within which the convective cells initiated. For the purpose of this study, we exclusively focused on

CI[3] occurring over land, while disregarding any CI over the ocean. We combined GOES-16 visible satellite imagery with NEXRAD data from KHGX radar (WSR-88D located in League City, Texas; NOAA National Weather Service (NWS) Radar Operations Center 1991), and two terminal Doppler weather radars near the George Bush Intercontinental and Hobby airports in Houston, Texas (TIAH and THOU, respectively). This allowed us to track the SBF, identifying its leading edge as a boundary separating fair weather bubbling cumulus clouds (or horizontal convective rolls) to the north or cumulonimbus clouds (post CI) at the frontal boundary from the relatively clear air mass to the south. We also examined satellite and radar images to ensure accurate delineation between the SBF and nearby cold-pool boundaries. During each IOP day, we tracked the SBF starting from its initial appearance as a coherent mesoscale boundary in the satellite and radar data until the point where its structure became too diffused to differentiate from nearby weak cold pool outflow boundaries. The spatial footprint of each SBF was recorded by manually outlining a polygon, considering the finite width and length of the frontal boundary and accounting for the uncertainty associated with satellite and radar-based location indicators for the fronts. This polygon was then saved as a list of latitude-longitude coordinates defining the boundary at 30 minute intervals. This interval was suitable for tracking the gradual progression of the SBF, except in cases when it merged with an outflow boundary from nearby convection. In such cases, polygons were recorded more frequently to capture the short-term changes in the SBF. To ensure the reliability of our subjective identification of the SBF location, we conducted a sensitivity analysis to account for minor spatial uncertainties in the position and width of the SBF boundary. In this analysis, we reclassified cells located within a 5-km distance on both sides of the SBF polygon boundary as 'SBF' cells. We repeated this process with a 10-km distance threshold. The aim was to assess whether variations in these thresholds would impact our findings. The sensitivity analysis revealed that our qualitative results remained consistent regardless of the distance threshold used. Furthermore, we validated the satellite and radar-based tracking of SBF propagation by comparing it with the timing of wind direction and speed changes recorded by the ASOS stations nearest to the fixed ARM sites.

We applied the filament spatiotemporal interpolation method (Boubrahimi et al. 2018) to estimate the SBF location every 5 minutes, aligning it with the frequency of CI data (roughly every 5 min,

[3]In this context, the term "CI" indicates the beginning time of a cell track when tracking convective clouds using KHGX radar data. For more details on cell tracking, please refer to section 2c.

coinciding with radar and satellite updates). Subsequently, using the location of each convective cell at the time of CI, we calculated its distance from the SBF, allowing differentiation between "maritime" and "continental" CI. Given the prevalence of convective cells that initiated in close proximity to the SBF, we classified all CI within 5 km of the SBF boundary as "SBF cells" to distinguish them from CI in purely continental or maritime air masses.

3. Results

a. Overview of the afternoon evolution of SBF and CI

During the inland propagation of the SBF, CI typically reached its peak between 1400 and 1500 LT (see Fig. 3). The distribution of cell lifetimes exhibited positive skewness, with a median lifespan of 32.5 minutes (Fig. 3a). In total, less than 14% of all tracked cells underwent either a merger or a split during their lifetime. Specifically, shallow cells had a median lifetime of 24 minutes, while transitioning cells had a median lifetime of 49 minutes. The hourly distribution of maximum cell area (Fig. 3b), maximum 20-dBZ echo-top height (Fig. 3c), and maximum cell reflectivity (Fig. 3d) did not reveal any discernible trends in their respective median values. However, the top quartile of both the maximum cell area and maximum 20-dBZ echo-top height, peaks between 1500 and 1700 LT (Fig. 3b and c), corresponding to the time when the SBF had already moved north of the ARM sites (cf. Figs. 4a and b). Many cells that initiated earlier had sufficient time to grow in size and attain their peak reflectivity, resulting in the time lag between the peak in CI and maximum area and 20-dBZ echo-top height values. The hourly distribution of maximum cell reflectivity, however, remained relatively constant throughout the analysis period (Fig. 3d).

The SBF typically moved northward (inland), exhibiting variations in both strength and extent of its areal coverage (Fig. 4). The only exception occurred on 26 August 2022 when scattered showers and thunderstorms developed along surface convergence from the sea breeze and a weak outflow boundary from prior convection. Subsequent interactions between the sea-breeze and convective outflow from widespread thunderstorms constrained the inland propagation of the SBF (Fig. 4c; dark violet line). The inter- and intra-day variability observed in Fig. 4c is likely a consequence of multi-scale interactions involving the synoptic flow, mesoscale gradients in surface fluxes, and local geographical characteristics, among other factors (Crosman and Horel 2010).

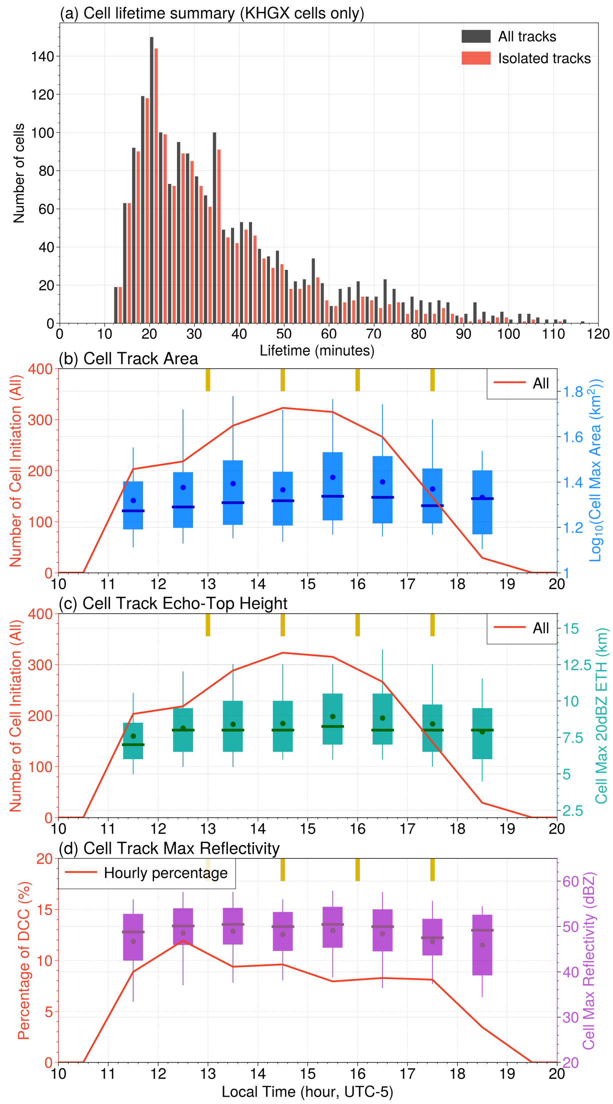

FIG. 3. Convective cell characteristics for the combined 15 TAMU TRACER IOPs analyzed in this study. Cells tracked for a minimum of 12 minutes were included in this analysis. (a) Distribution of cell lifetimes (minutes). Gray bars correspond to all cells, while red bars represent cells that remained isolated throughout their lifetime. Hourly boxplots for (b) Maximum cell area (logarithmic scale), (c) Maximum 20-dBZ echo-top height (km), (d) Maximum composite reflectivity (dBZ). Red line in (b) and (c) represents the hourly cell initiation count, whereas in (d), it signifies the hourly percentage of cells that developed into deep convection. Golden bars on the top axis represent the typical radiosonde launch times from ARM sites. Cell sample size includes only those identified at or on either side of the SBF within a 150 km range from the KHGX radar between 1100 and 1900 LT.

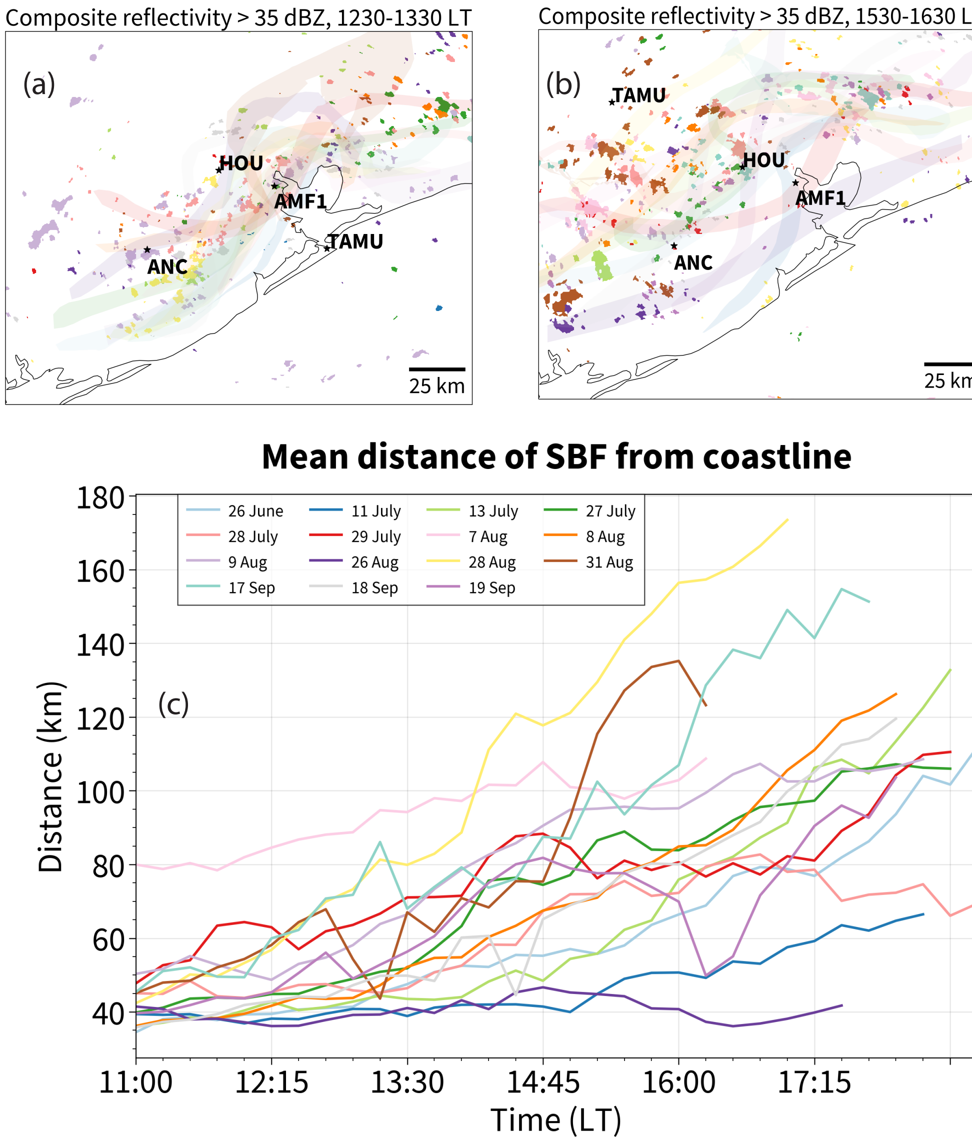

FIG. 4. Summary of the location of SBF boundary (transparent shaded region) and convective cells with ≥ 35 dBZ composite reflectivity (solid filled contours) during the early afternoon (a) and late afternoon (b), combining all 15 TAMU TRACER IOP days. The early and late afternoon timings align with the radiosonde launch times by the TAMU crew. The 35-dBZ composite reflectivity threshold indicates the location of precipitation core of each convective cell. The time series in (c) illustrates the mean distance of the SBF boundary from the coastline for each IOP day.

The analysis of cell initiation density (count of cell tracks that started within a lon-lat grid cell of size 0.14°× 0.13°) revealed two prominent hotspots, located to the east-northeast (east of the AMF1 site) and southwest of the Houston metropolitan region (around the ANC site; Fig. 5a). These hotspots indicate the preferential CI locations due to SBF convergence, consistent with the climatological trend reported by Tuftedal et al. (2023) in their multi-year analysis of sea-breeze convection in and around the Houston region. The timing of peak CI (1300–1600 LT; see Fig. 3b) also aligns with their findings and coincides with the typical passage of the SBF through the hotspots. The mean values of cell area and 20-dBZ echo-top height exhibited slightly higher values over the southwestern hotspot (near the ANC site) and also in the region northwest of the AMF1 site, potentially due to mature deep convective clouds moving across these areas later in time (Fig. 5b and c).

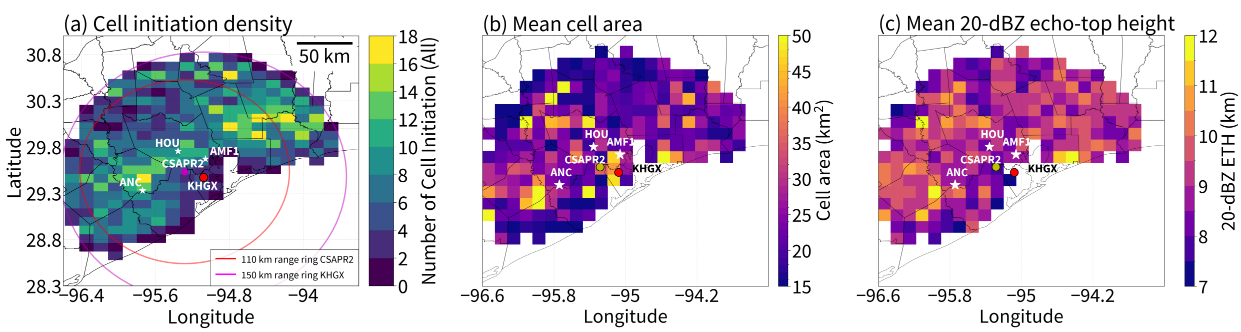

Fig. 5. Spatial heatmaps of cell attributes for cells that initiated over land, within a 150-km range from the KHGX radar during the analyzed IOP days (refer Table 1). (a) Gridded count of cell initiation, (b) Gridded mean cell area, and (c) Gridded mean 20-dBZ echo-top height. Heatmaps in (b) and (c) illustrate mean values for all cell tracks at all times in their lifetime. Therefore, slow moving cells may have contributed to the same bin multiple times.

b. Overview of spatiotemporal environmental heterogeneity across air mass regimes

To quantify the thermodynamic variability across the SBF, we categorized TAMU and ARM sounding data according to the time of radiosonde launch: early afternoon (1230–1400 LT) and late afternoon (1530–1900 LT). The SBF contributed to the presence of distinct, nonstationary mesoscale air masses in the Houston area, allowing us to sample the differences between air masses, but also the heterogeneity within an air mass when there were multiple observing sites in the same air mass. Consequently, this subsection delves into the environmental heterogeneity by considering the sites from which the soundings were launched.

To visualize the differences in thermodynamic environments, we computed composite profiles of sounding data from each site at the time closest to the TAMU radiosonde separately for early and late afternoon periods. We plotted the Skew$T$-log$p$ diagram by interpolating and averaging the dry bulb and dewpoint temperature profiles onto a 5 m vertical resolution AGL grid for each site (Figs. 6a and b). In the early afternoon composite, the TAMU profiles (primarily in the maritime air mass) exhibited the highest dewpoint temperature within the lowest 50-hPa layer. However, moisture decreased rapidly above the 950 hPa level, resulting in the lowest dewpoint temperature in TAMU soundings between 950 and 700 hPa. Additionally, a combination of overall lower temperature and moisture within the lowest 100-hPa layer at the TAMU site led to the lowest values of mixed-layer convective available potential energy (ML CAPE) at the TAMU site.

On the other hand, the late afternoon sounding composite revealed a moisture deficit at the TAMU site within the lowest 100-hPa layer, along with a substantial dry layer in the mid-levels between the 600 and 400-hPa levels (Fig. 6b). The surface equivalent potential temperature ($\theta_{e,sfc}$) of the continental air mass at the TAMU site was considerably higher than the ARM sites. However, the higher θ_e air was very shallow, so when considering the drier mixed layer at the TAMU site, mixed-layer θ_e was lower at the TAMU site. The maritime air mass (ARM sites) was drier compared to continental air mass (TAMU) between the 900 and 650-hPa levels. This could partly be due to subsidence in the sinking branch of the sea breeze circulation. Despite differences between air masses and observing sites, ML CAPE generally decreased everywhere later in the day due to reduced solar insolation and mixing of dry continental air with moist maritime air mass as the SBF moved farther inland (compare Figs. 6a and b).

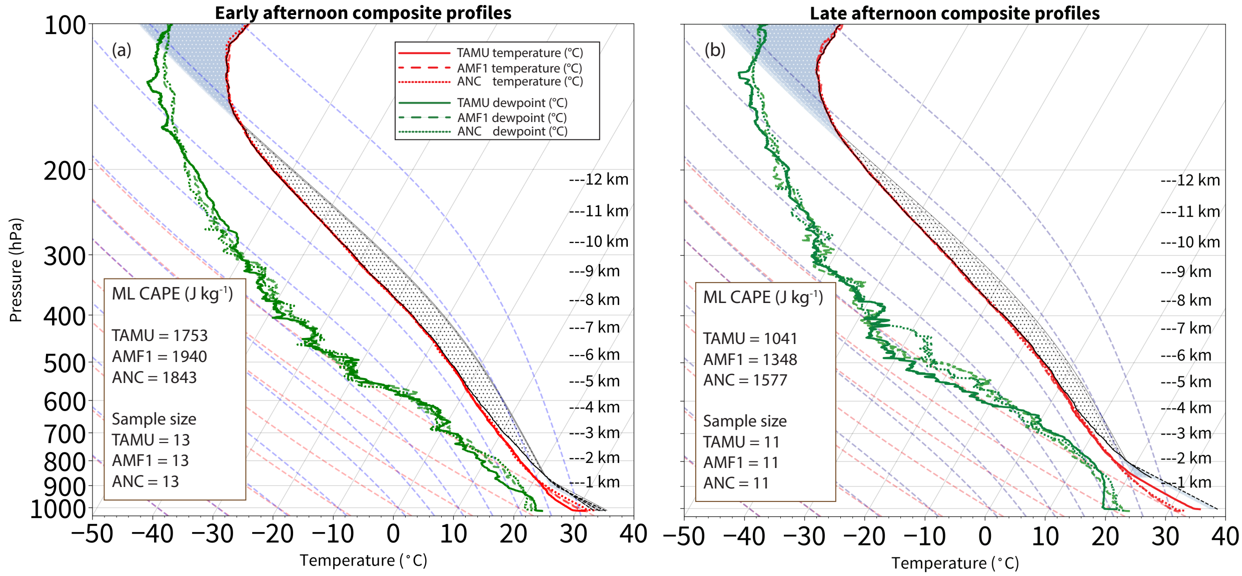

FIG. 6. Skew$T$-log$p$ diagrams of composite environmental profiles at TAMU (solid line), AMF1 (dashed), and ANC (dotted) sites during radiosonde launches in (a) early afternoon (1230–1400 LT) and (b) late afternoon (1530–1900 LT). Parcel path (solid gray line) in (a) and (b) corresponds to the lowest 100 hPa mixed-layer parcel in the TAMU sounding data. Virtual temperature profiles are shown as dashed black lines.

Thermodynamic heterogeneity between early and late afternoon air masses at the three sounding sites can also be visualized by plotting the composite profile differences of potential temperature, relative humidity, and undiluted parcel buoyancy (Fig. 7). This comparison helps mitigate variability in overall synoptic conditions across days and offers further insight into the variability of thermodynamic conditions. For example, in the early afternoon the largest differences in all three thermodynamic variables were found within the surface–3 km layer between the TAMU and ANC sites (Fig. 7c). The low-level air mass heterogeneity between these two sites persisted in the late afternoon, with the largest differences confined to the surface–2 km layer (Fig. 7d). The warm and dry continental air mass at the TAMU sites in the late afternoon also resulted in a larger reduction in parcel buoyancy when compared with both the ARM sites (Fig. 7b and d). However, the differences in potential temperature and relative humidity reached their peak magnitude between the TAMU and AMF1 sites at mid-to-upper levels (between 4 and 12 km AGL; Fig. 7b). The ARM sites had the least variability in the early and late afternoon, and with the cooling and moistening at the ANC site in late afternoon, the low-level differences in potential temperature and relative humidity were further reduced (Fig. 7e and f).

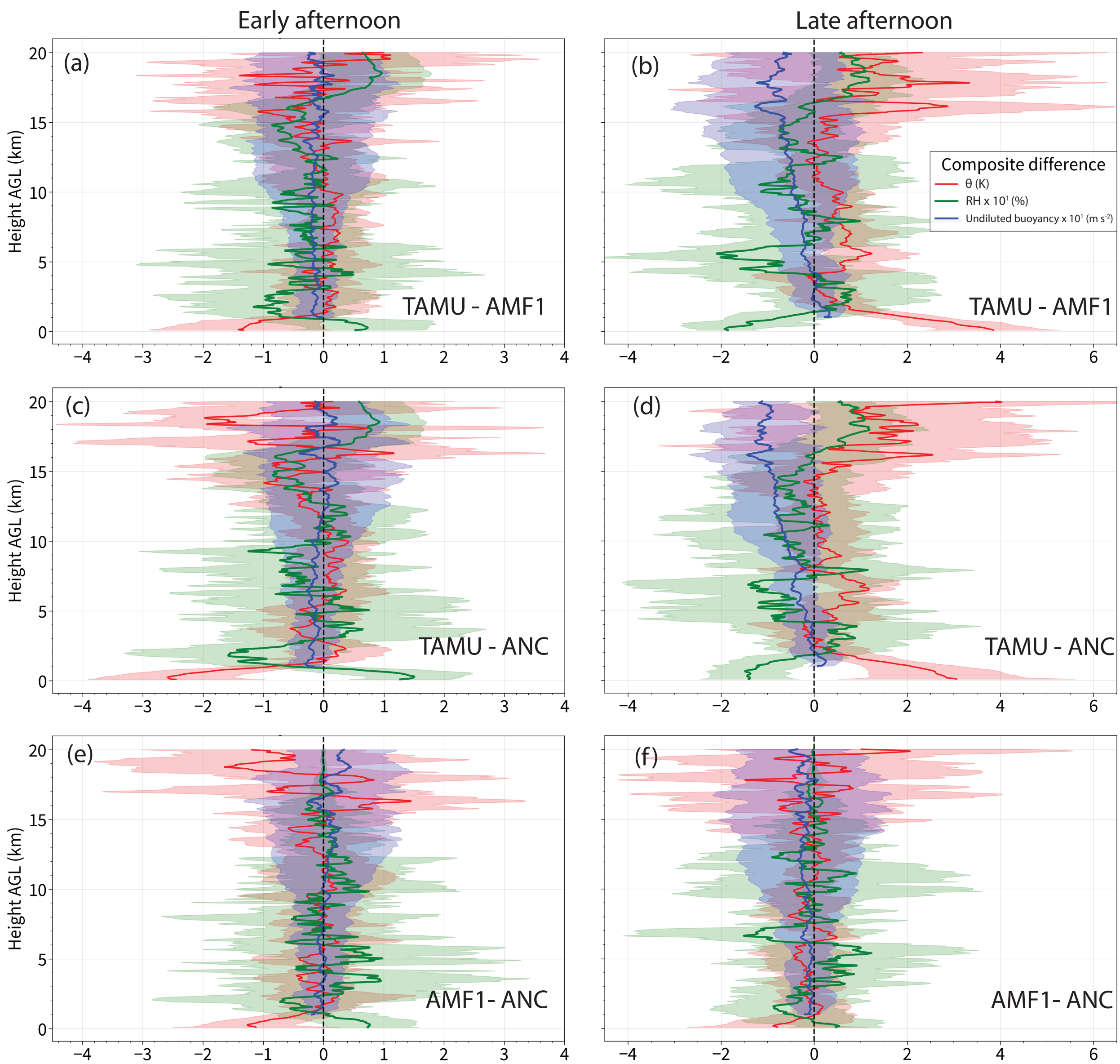

FIG. 7. Vertical profiles for composite mean (solid line) and ±1 standard deviation around the mean of differences (shaded) for potential temperature (θ; red), relative humidity multiplied by 10 ($\mathrm{RH} \times 10^1$; green), and undiluted parcel buoyancy multiplied by 10 (blue). (a) Differences between early afternoon TAMU and AMF1 sounding data, (b) same as (a) except for late afternoon sounding data, (c) differences between early afternoon TAMU and ANC sounding data, (d) same as (c) except for late afternoon sounding data, (e) differences between early afternoon AMF1 and ANC sounding data, (f) same as (e) except for late afternoon sounding data. Dashed black vertical line indicates a difference of zero. The vertical profiles were generated after smoothing the data using a rolling mean with a 100-m window.

Site-specific differences between sounding-derived parameters reveal that the maritime air mass sampled by the TAMU soundings (from the sea breeze) had lower values of total precipitable water (TPW), mixed-layer entraining CAPE (ML ECAPE), and PBL height compared to the ARM sites during the early afternoon deployments (Fig. 8a,c, and d). However, the maritime air mass sampled at the AMF1 site in the early afternoon (from the bay breeze) had the maximum TPW. As the SBF boudnary passed over the fixed ARM sites and mixed with the preexisting air masses at those locations, the thermodynamic characteristics became more homogeneous at the AMF1 and ANC sites in the late afternoon (Fig. 8a–d). The dry air mass encountered at the TAMU site during late afternoon played a significant role in the entrainment-driven dilution of the parcel buoyancy. This led to substantial reductions of ML ECAPE values compared to those observed at the ARM sites (Fig. 8c).

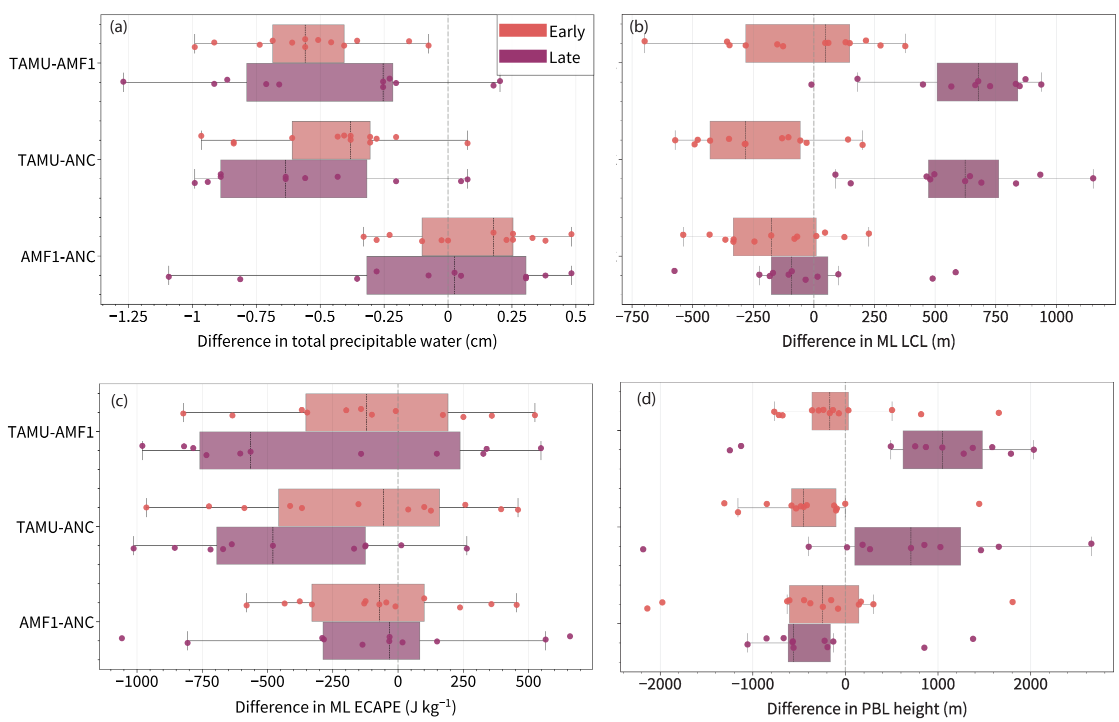

Fig. 8. Boxplot distribution of the difference in (a) total precipitable water, (b) ML LCL, (c) ML ECAPE, and (d) PBL height values between TAMU, AMF1, and ANC sounding data, grouped by early (orange) and late afternoon (purple) radiosonde measurements. Individual data points contributing to each distribution are depicted as dots overlaying the boxplots, with the median value denoted by the dashed black line within each box. The dashed grey vertical line in each panel plot indicates a difference of zero.

Partitioning the soundings by air mass provides better understanding of the thermodynamic variability within similar air masses while also revealing disparities between different air masses during the same time periods. With the exception of the AMF1 site, the dominant air mass changed between the early and late afternoon soundings as the SBF passed. The close presence of Galveston Bay led to a much earlier transition to maritime air at the AMF1 site, where a bay breeze typically reached the site at least 3 hours before the sea breeze (Dié Wang, personal communication, January 2023). Therefore, AMF1 was an ideal site to investigate heterogeneity within the maritime air mass.

The contrasting thermodynamic properties between the sea and bay breeze air masses were evident in the significantly different distribution of ML CAPE values during the early afternoon maritime soundings at the TAMU and AMF1 sites, respectively (Fig. 9a). The median ML CAPE for TAMU soundings was 1780 J kg^{-1}, while for AMF1 soundings, it was 2118 J kg^{-1}. Surprisingly, the ML CAPE values for the continental air mass sampled at the ANC site were similar to the TAMU site. We initially anticipated a larger variability between continental and maritime air masses than within different maritime air masses from distinct sources. A possible explanation for this unexpected result could be the influence of prior convective outflow nearby, leading to low-level moistening earlier in the day before the sea breeze reached the ANC site.

During the late afternoon radiosonde launches, both ARM sites were in a maritime air mass. The distribution of ML CAPE values had a notable overlap between the AMF1 and ANC sites (both maritime), whereas at the TAMU site (continental) the distribution was negatively skewed, with a median value of 1170 J kg^{-1}, considerably lower than the median ML CAPE at the AMF1 (1415 J kg^{-1}) and ANC (1628 J kg^{-1}) sites. The late afternoon maritime air mass sampled at the AMF1 site also had the largest variability which is most likely an outcome of the complex interactions of sea and bay breeze with convective outflow boundaries from nearby convection. A comparison of mean values for other environmental parameters, categorized based on the launch site and time of the day, is provided in Tables 2 and 3. Throughout both the early and late afternoon, significant moisture differences persisted between the TAMU and ANC sites. In the early afternoon, these differences manifested in the mean RH within the 850-700 hPa layer, which roughly corresponds to the active cloud-bearing region (the layer located between the height of the LFC and 1.5 km above it; see Lock and Houston 2014) for these data. As the day progressed, the contrast in mean boundary layer RH between the two sites became increasingly pronounced. Besides CAPE, differences in the thermodynamic properties of air masses sampled at the TAMU and ARM sites were also evident in the boundary layer depth, LCL height, 0–3 km lapse rate, and effective inflow layer depth (the contiguous layer wherein lifted parcels would have at least 100 J kg^{-1} of CAPE and CIN < -250 J kg^{-1}; see Thompson et al. 2007).

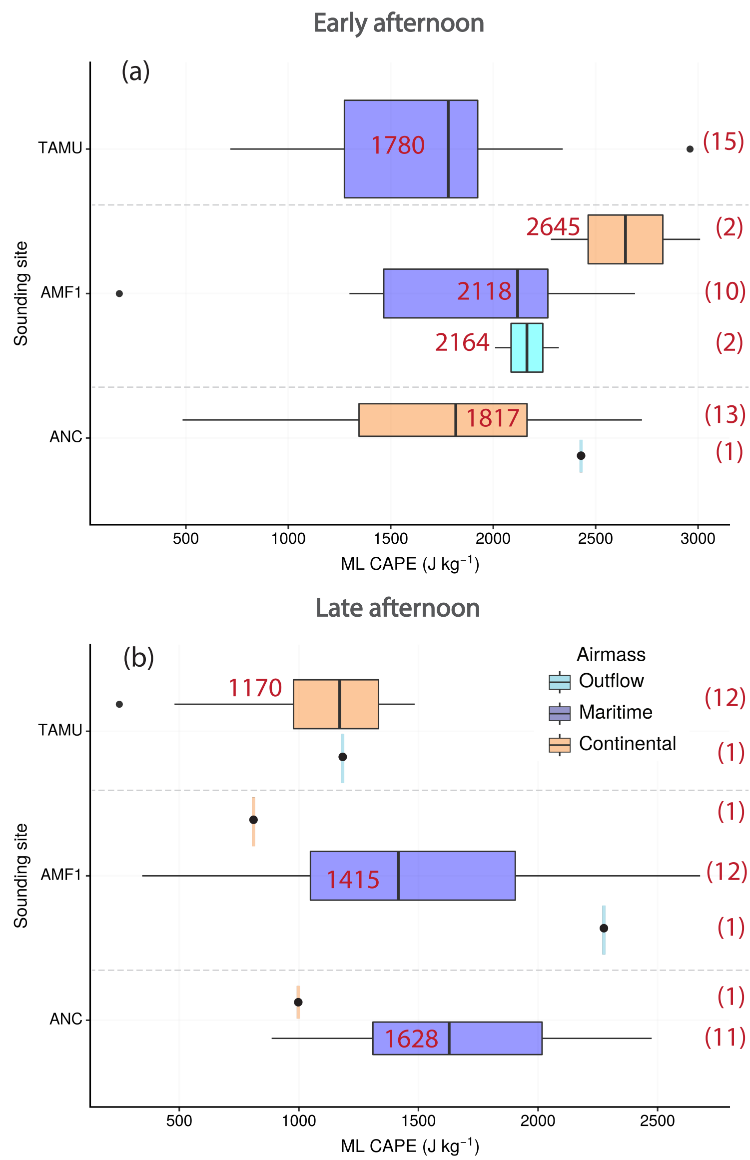

451 FIG. 9. Boxplots of ML CAPE (lowest 100 hPa mixed-layer parcel) depicting thermodynamic variability within and across maritime (violet), continental (orange), and outflow (cyan) air masses at TAMU, AMF1, and ANC sites during (a) early and (b) late afternoon environmental soundings. Median ML CAPE values for each distribution are indicated next to the respective boxplots. Sample sizes for each category are shown in parentheses on the right.

Table 2. Environmental metrics for soundings launched from different sites (and air masses) during the early afternoon deployments. The Kruskal-Wallis test was performed to test whether the mean values of environmental parameters were significantly different among the three launch sites at an α level of 0.05. If the Kruskal-Wallis test indicated a difference, the Dunn test was performed for pairwise comparisons between launch sites to find out which two sites were statistically significantly different at α = 0.05. The * symbol denotes sites with statistically significant difference in parameters. In instances where two sites were similar, but both differed from the third site, a † symbol is used. Table entries represent the mean value (bold text) ± the standard error. Sample sizes for each site are indicated within parentheses below the corresponding site name.

Environmental metric	**Early afternoon**		
	TAMU (15)	AMF1 (14)	ANC (14)
Moisture			
Total precipitable water vapor (cm)	**4.77** ± 0.21	**5.00** ± 0.29	**4.99** ± 0.28
Mean PBL RH (%)	**74.21** ± 4.2	**72.84** ± 5.32	**72.98** ± 4.41
Mean RH 850–700 hPa layer (%)	**63.82*** ± 6.26	**70.74** ± 7.08	**73.99*** ± 4.93
Mean RH 700–500 hPa layer (%)	**50.99** ± 6.4	**52.75** ± 9.98	**50.33** ± 9.24
Temperature and instability			
CAPE for SFC or MU parcels (J kg^{-1})	**3532** ± 517	**3850*** ± 638	**2923*** ± 421
CIN for ML parcels (J kg^{-1})	**-27** ± 16	**-19** ± 13	**-11** ± 7
LFC for ML parcels (m)	**1653** ± 307	**1618** ± 480	**1754** ± 389
LCL for ML parcels (m)	**1055*** ± 95	**1199** ± 216	**1372*** ± 194
Depth of boundary layer (m)	**1312*** ± 110	**1371** ± 330	**1722*** ± 369
EL for ML parcels (m)	**13789** ± 448	**13698** ± 969	**13708** ± 629
0 °C layer altitude for ML parcels (m)	**4893** ± 100	**4906** ± 125	**4942** ± 124
Lapse rate 0–3 km AGL (K km^{-1})	**7.66*** ± 0.14	**7.84** ± 0.36	**8.14*** ± 0.41
Lapse rate 3–6 km AGL (K km^{-1})	**5.89** ± 0.17	**5.92** ± 0.14	**5.96** ± 0.19
Lapse rate 850–500 hPa layer (K km^{-1})	**6.01** ± 0.15	**6.04** ± 0.15	**6.09** ± 0.15
Lapse rate 700–500 hPa layer (K km^{-1})	**5.84** ± 0.19	**5.88** ± 0.17	**5.94** ± 0.25
Lifted index for ML parcels	**-3.93** ± 0.53	**-4.21** ± 0.79	**-4.14** ± 0.68
Wind and shear			
SRH in effective inflow layer (m^2 s^{-2})	**7** ± 14.85	**23.14** ± 18.76	**8.51** ± 17.16
SRH in 0–3 km layer (m^2 s^{-2})	**17.65** ± 23.11	**24.74** ± 20.89	**21.41** ± 19.59
Bulk shear in effective inflow layer (m s^{-1})	**2.44** ± 0.84	**3.34** ± 1.69	**4.26** ± 1.55
Bulk shear in 0–1 km layer (m s^{-1})	**2.20** ± 0.62	**3.50** ± 1.47	**2.91** ± 0.54
Bulk shear in 0–6 km layer (m s^{-1})	**4.39** ± 1.43	**5.68** ± 1.43	**5.48** ± 1.85
Other			
Depth of effective inflow layer (m)	**1106*** ± 188	**1577*†** ± 383	**1839*†** ± 292

TABLE 3. Same as Table 2 except for soundings launched during late afternoon deployments.

Environmental metric	**Late afternoon**		
	TAMU (13)	AMF1 (14)	ANC (12)
Moisture			
Total precipitable water vapor (cm)	**4.64** ± 0.2	**4.85** ± 0.32	**4.92** ± 0.23
Mean PBL RH (%)	**60.79*** ± 4.25	**65.91** ± 5.1	**68.60*** ± 4.3
Mean RH 850–700 hPa layer (%)	**74.74** ± 4.01	**68.31** ± 6.59	**71.05** ± 5.51
Mean RH 700–500 hPa layer (%)	**48.90** ± 9.35	**55.37** ± 10	**48.91** ± 9.33
Temperature and instability			
CAPE for SFC or MU parcels (J kg^{-1})	**2638** ± 455	**3340** ± 466	**2762** ± 384
CIN for ML parcels (J kg^{-1})	**-20** ± 13	**-51** ± 22	**-33** ± 23
LFC for ML parcels (m)	**2389** ± 262	**2104** ± 399	**2040** ± 405
LCL for ML parcels (m)	**1930*** ± 232	**1382***† ± 166	**1417***† ± 156
Depth of boundary layer (m)	**1962*** ± 671	**1132*** ± 233	**1440** ± 428
EL for ML parcels (m)	**13032** ± 486	**13268** ± 731	**13673** ± 442
0 °C layer altitude for ML parcels (m)	**4964** ± 115	**4942** ± 99	**4980** ± 85
Lapse rate 0–3 km AGL (K km^{-1})	**8.75*** ± 0.47	**7.73*** ± 0.27	**7.95** ± 0.51
Lapse rate 3–6 km AGL (K km^{-1})	**5.9** ± 0.26	**5.96** ± 0.17	**5.95** ± 0.21
Lapse rate 850–500 hPa layer (K km^{-1})	**6.32** ± 0.28	**6.18** ± 0.21	**6.17** ± 0.23
Lapse rate 700–500 hPa layer (K km^{-1})	**5.82** ± 0.33	**5.93** ± 0.2	**5.96** ± 0.22
Lifted index for ML parcels	**-2.46*** ± 0.59	**-3.36** ± 0.92	**-3.75*** ± 0.72
Wind and shear			
SRH in effective inflow layer (m^2 s^{-2})	**3.68** ± 16.33	**29.68** ± 21.82	**15.97** ± 11.5
SRH in 0–3 km layer (m^2 s^{-2})	**6.65*** ± 21.43	**42.91*** ± 25.62	**26.32** ± 16.14
Bulk shear in effective inflow layer (m s^{-1})	**3.36** ± 1.78	**3.86** ± 1.67	**3.94** ± 1.52
Bulk shear in 0–1 km layer (m s^{-1})	**4.22** ± 1.04	**4.11** ± 1.07	**2.70** ± 1.08
Bulk shear in 0–6 km layer (m s^{-1})	**4.44** ± 1.72	**6.87** ± 2.05	**6.01** ± 1.89
Other			
Depth of effective inflow layer (m)	**1894** ± 424	**1323** ± 435	**1860** ± 200

To incorporate the effect of dry air entrainment on updraft dilution, we computed the nondimensional entraining CAPE ($\tilde{E}_A$) for each air mass regime, following the analytic formulation proposed by Peters et al. (2023). This approach avoids making assumptions regarding the updraft radius or entrainment rate and rather determines the latter directly from an environmental sounding. We found that both the distribution and the median value of $\tilde{E}_A$, which represents the fraction of undiluted CAPE realized by an updraft, were comparable (~0.55) for both continental and maritime air masses (Fig. 10). Therefore, the updraft parcels in the maritime and continental air masses experienced substantial dilution along their trajectories. In contrast, parcels in the outflow air mass had a lesser impact from entrainment, with a median value of approximately 0.6.

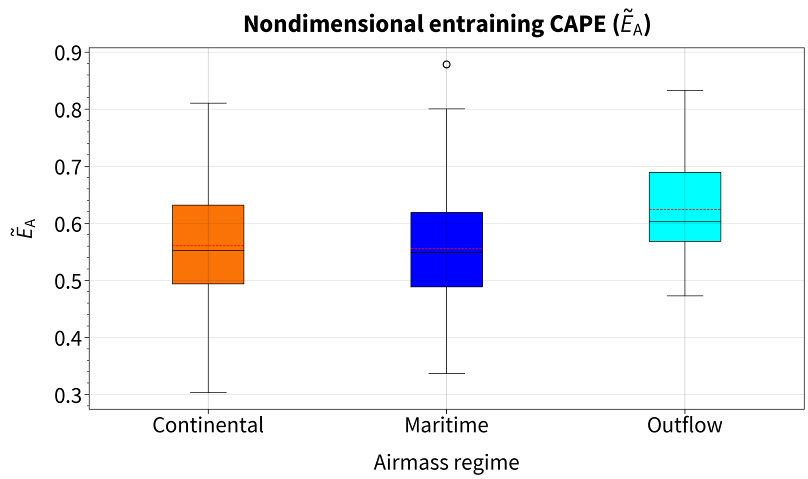

FIG. 10. Nondimensional entraining CAPE ($\tilde{E}_A$) for all soundings from TAMU, AMF1, and ANC sites, categorized based on the air mass sampled by the radiosondes. $\tilde{E}_A$ represents the fraction of undiluted CAPE realized by an updraft (Peters et al. 2023). Solid black and dashed red lines in the shaded part (inter-quartile range) of the boxplots indicate the median and mean, respectively. Sample sizes are indicated within parentheses on the x axis.

c. *Overview of convective cell characteristics across air mass regimes*

1) KHGX cell tracking statistics

Although composite reflectivity alone may not always be the best estimator of convective updraft intensity, trends in composite reflectivity can still provide valuable insights into the overall evolution of cell intensity. We define composite reflectivity as the maximum radar reflectivity observed anywhere within the three-dimensional volume of the tracked cell. To investigate the possible effect of air mass heterogeneity on cell characteristics, we partitioned the cell tracks into shallow and transitioning cloud categories (refer section 2c). To ensure the robustness of this analysis, we exclusively considered cells that were tracked over a minimum of four consecutive KHGX PPI scans (approximately $\geq$ 18 minutes). This filtering step aimed to exclude short-lived cells that could potentially introduce noise to the dataset. The number of cells contributing to the mean composite reflectivity at any specific time varied throughout the analysis period. As a result, the time series plots were terminated once the cell sample size in any one air mass regime fell below 10, ensuring that the analysis is based on a sufficient number of cells for robust conclusions. In section 3b, we focused on site-specific environmental variability. Here, we pivot to examining the characteristics of convective cells initiating in varied air masses. This shift allows us to quantify how the heterogeneity of air masses influences the evolution of convective cell properties.

A clear contrast is evident in the time series of composite reflectivity between shallow and transitioning clouds (Fig. 11a and b). As expected, transitioning clouds in each air mass regime had a larger mean composite reflectivity compared to their shallow counterparts. When comparing just the shallow clouds, those that initiated at or in the immediate vicinity of the SBF exhibited the highest mean composite reflectivity (41–44 dBZ) throughout the analysis period. This was followed by shallow clouds originating within maritime (36–40 dBZ) and continental (30–35 dBZ) air masses, respectively. Transitioning clouds that initiated at or near the SBF also had a slightly larger mean composite reflectivity up to the first 65 minutes. Up to 30 minutes in the life cycle, the 95% confidence interval band around the mean composite reflectivity had a significant overlap for continental and maritime cells. However, past the 30-minute mark, maritime cells exhibited a slightly larger mean composite reflectivity for the remainder of the analysis period.

Another commonly employed metric for assessing and distinguishing convective intensity is the echo-top height derived from radar reflectivity. However, the time series of the maximum

20-dBZ echo-top height in both shallow and transitioning clouds across various air mass regimes shows no significant differences (Fig. 11c and d). Despite this lack of distinction, the higher composite reflectivity observed in both shallow and transitioning clouds at the SBF, compared to their counterparts in the maritime and continental air masses, suggests the potential influence of sea-breeze dynamics on convection and associated warm and cold-cloud processes. It is plausible that additional moisture and lifting at the leading edge of the SBF may have altered the rate of microphysical processes (Michelle Spencer, University of Oklahoma, 2023, personal communication). Furthermore, the dynamic forcing at the leading edge of the SBF combined with the complex mixed and ice-phase microphysical processes can also alter the drop size distribution, possibly leading to the enhanced reflectivity observed in the SBF clouds (Hopper et al. 2020; Suh et al. 2021).

Rapid growth of cloud base area at the time of CI or pre shallow-to-deep transition is a good predictor of maximum cell area and cell longevity (Wilhelm et al. 2023). We found that only transitioning cells exhibited a distinctive growth in cell area across the air masses (Fig. 11e and f). Maritime cells exhibited the highest values of average cell area, which was also positively correlated to the cell track duration (not shown). Furthermore, the mean lifetime of maritime cells (62 minutes) was higher than the continental cells (55 minutes). It is possible that the cold pool modified air mass reinforced updraft redevelopment in long-lived maritime cells (Houston and Wilhelmson 2011).

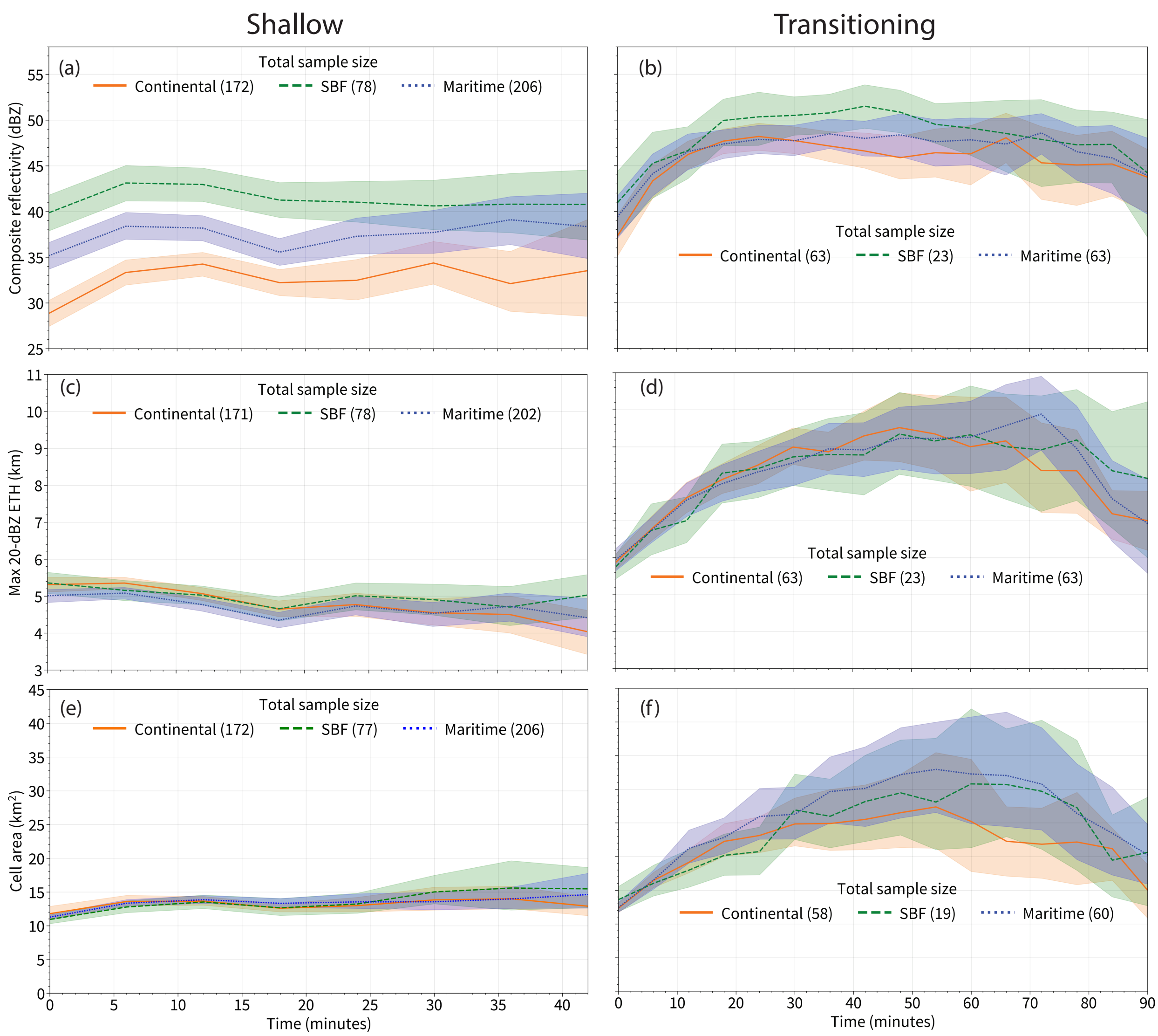

FIG. 11. Time series of mean values of composite reflectivity (a-b), maximum 20-dBZ echo-top height (c-d), cell area (e-f), categorized based on the air mass in which they initiated. Panel plots in the left and right columns correspond to shallow and transitioning cells, respectively. Colored lines represent the mean, and the shaded area represents the 95% confidence interval around the mean. The total sample size for each air mass category is included within parentheses in the legend. The upper limit of track duration (x-axis) was chosen to ensure at least five samples contributed to composite reflectivity values for all three air mass categories.

2) CSAPR2 cell tracking statistics

During the TRACER field campaign, the warm season subtropical environments in southeast Texas were characterized by a predominance of single-cell, ordinary convection. These cells had a relatively short lifespan, with approximately 70% of the cells lasting less than 45 minutes (see Fig. 3a). CSAPR2 RHI scans provide both enhanced temporal and vertical spatial resolution of a subset of the convective cells during TRACER.

However, the CSAPR2 RHI data had limitations due to the inability to sample all convective cells simultaneously. The automated CSAPR2 cell tracking strategy (Lamer et al. 2023) allowed sampling of only one target cell at a time, leading to a decision of whether to continue scanning the same cell in the next scan bundle or switch to another cell in the domain. As a result, the automated cell tracking algorithm often abandoned a cell midway in its life cycle if another target cell was identified according to the automated set of rules. This inconsistency in cell tracking, coupled with the physical limitation of CSAPR2's smaller maximum unambiguous radar range, resulted in a much smaller dataset of transitioning cells available for this analysis. Consequently, we compare vertical profiles of maximum Z_H, Z_{DR}, and K_{DP} instead of comparing the evolution of time series of these radar variables.

There were at least two notable differences between the KHGX and CSAPR2 composite reflectivity (Fig. 12a, respectively). The first difference was related to the air mass regime with the maximum composite reflectivity value. Although the CSAPR2 near-surface composite mean was similar across all three air masses, the most significant disparity occurred between 2500 and 3000 m above radar level (ARL), where the continental cells reached the largest value. The second difference was the larger absolute maximum value of the mean composite reflectivity in CSAPR2 continental cells (~55 dBZ), compared to the maximum value in the KHGX data (~49 dBZ). This is likely due to the limited CSAPR2 sample size and/or differences in resolution or radar frequency. Direct comparison of composite reflectivity between the CSAPR2 vertical profiles and the NEXRAD time series (see Fig. 11b) is unfair because of the disparities in spatiotemporal resolution and constraints introduced by partial sampling of the cell life cycle by CSAPR2. However, in qualitative terms, the composite reflectivity in continental cells, as observed in the NEXRAD time series, never exceeded that of maritime cells by more than 1 dBZ. The most likely explanation for this discrepancy is the limited sample size of continental cells in CSAPR2 data (refer cell count distribution in Fig. 12d) or the coarser vertical resolution of gridded NEXRAD data. To assess the extent of variability in maximum cell composite reflectivity, we examined three example cases of deep convection (one in each air mass regime) that were scanned by both radars. While the CSAPR2 and KHGX reflectivity profiles generally followed the same overall trend, differences in excess of 10 dBZ in reflectivity values were observed at times (Fig. 13). Except for a few RHI sweeps in the continental cell, the CSAPR2 reflectivity values were consistently higher than those from KHGX. Additionally, a considerable RHI to RHI variability was evident in all three examples, capturing the fast temporal-scale fluctuations in cell reflectivity and fine-scale microphysical processes as they evolve in deep convective updrafts, which would otherwise have been missed in KHGX PPI volumetric updates.

The analysis of composite mean Z_{DR} and K_{DP} vertical profiles revealed significant microphysical differences among storms across different air masses. In continental and SBF cells, the peak Z_{DR} reached 5 dB, indicating the presence of large oblate raindrops (Fig. 12b). The peak Z_{DR} values, however, occurred at different altitudes in continental cells (around 1000 m ARL) compared to SBF cells (around 500 m ARL). A sharp decrease in near-surface Z_{DR} below these peaks in both air mass regimes suggests possible raindrop breakup or evaporation affecting the drop size distribution close to the ground. On the other hand, the Z_{DR} profile in maritime cells remained more constant with height (around 3 dB between 0 and 3000 m ARL), which could be attributed to a lower evaporation rate in the humid maritime boundary layer. Using a 1-dB threshold to identify the vertical extent of Z_{DR} columns, cells within the continental air mass exhibited the tallest Z_{DR} columns, extending up to an altitude of 7 km ARL, at least 1 km higher than the maritime and SBF storms.

For K_{DP} profiles, maritime and SBF cells showed overlap throughout, reaching a maximum of around 1.9 deg km^{-1} at approximately 3000 m ARL, with slightly higher near-surface K_{DP} values in SBF cells. The K_{DP} profile for continental cells followed a similar trend to the other two air mass regimes at upper levels before significantly deviating below 1500 m ARL. The K_{DP} profile for continental cells exhibited a sudden spike at lower altitudes, with the peak value reaching around 1.8 deg km^{-1} around 500 m ARL. This may suggest that precipitation in continental storms was characterized by a higher concentration of smaller raindrops. However, the limited sample size of continental cells below 500 m ARL could have skewed the Z_{DR} and K_{DP} values towards higher values at low levels.

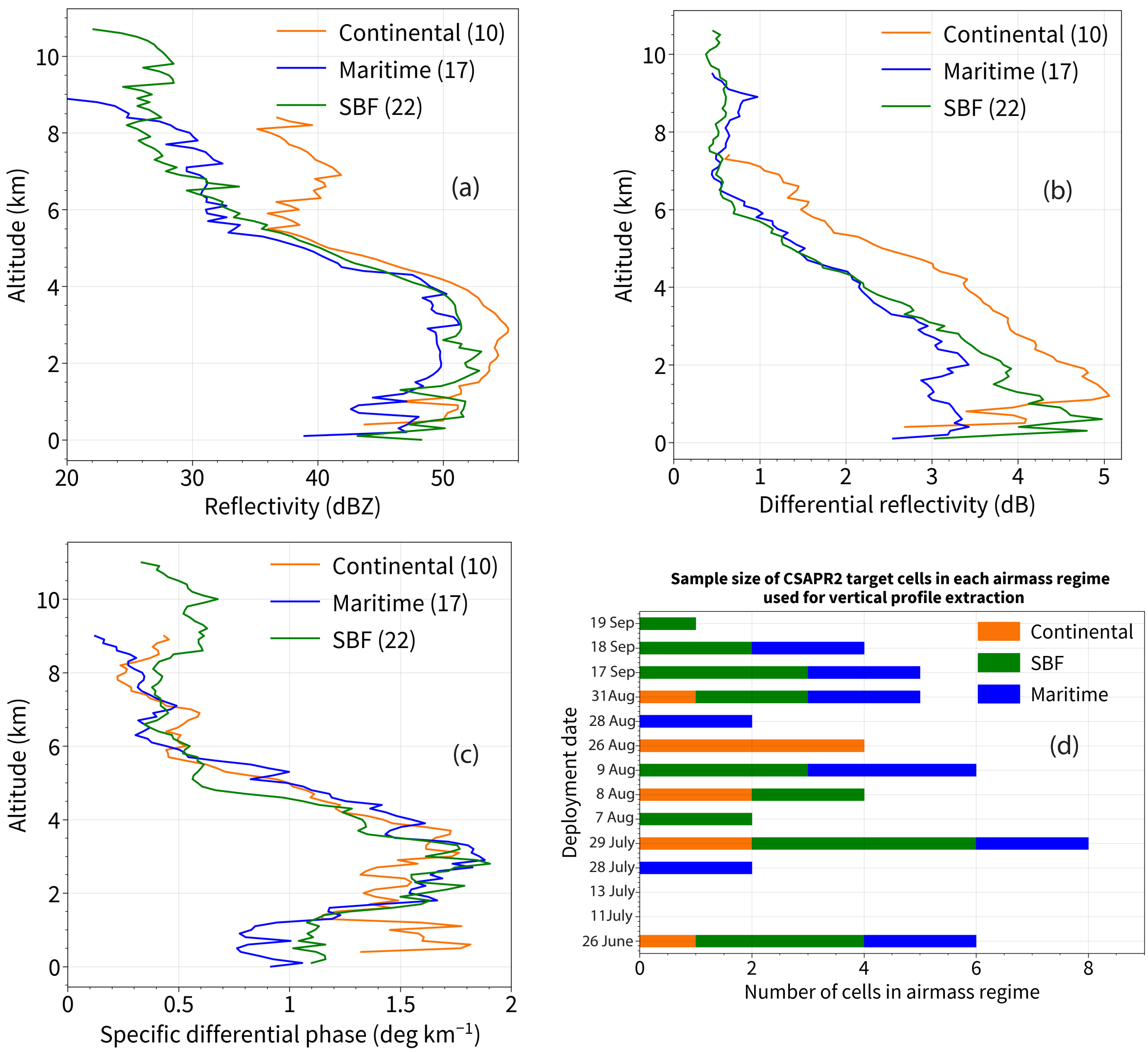

593 FIG. 12. Composite mean vertical profiles of (a) Maximum reflectivity, (b) Maximum Z_{DR}, and (c) Maximum integrated K_{DP} for cells observed by CSAPR2. The numbers within parentheses in (a), (b), and (c) represent the cell count for each air mass regime. A minimum of five samples were used for averaging at each vertical level. (d) Cell count per air mass for each deployment, for cells used in vertical profile extraction.

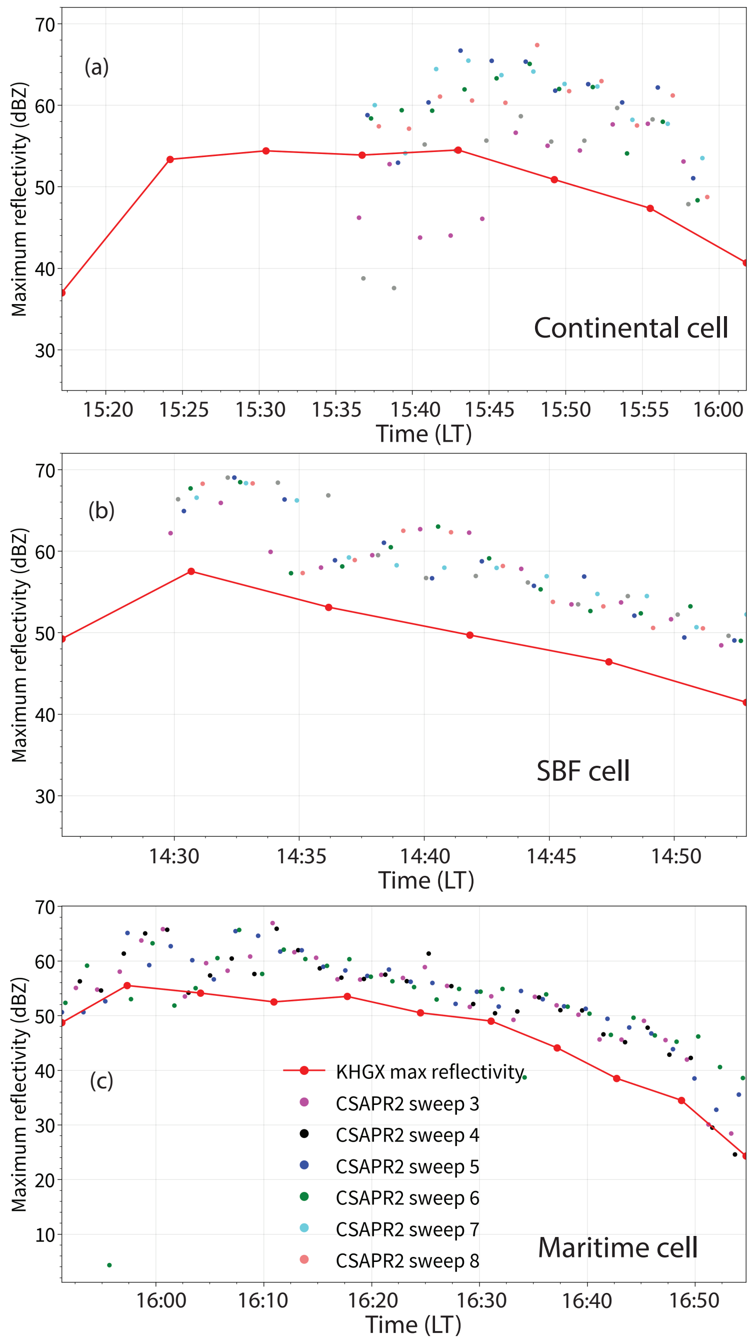

FIG. 13. Evolution of maximum radar reflectivity observed through KHGX PPI volume scans (solid line with markers; red color) and CSAPR2 RHI scans (scatter points) for three example cells that initiated in (a) continental air mass, (b) at the SBF boundary, and (c) maritime air mass. CSAPR2's faster RHI scans enabled retrieval of multiple maximum reflectivity values along different cross-sections within the same convective cell, resulting in multiple CSAPR2 sweeps between two KHGX PPI scans.

d. Statistical significance of environmental conditions for cell attributes

The analysis presented heretofore explored the differences in thermodynamic environments and cell characteristics independently of each other. Now, our focus shifts to understanding how the continental and maritime air mass regimes may affect convective cells. In order to test whether continental or maritime cells experienced significantly different environmental conditions, we assigned the closest radiosonde in time and space to each cell, so long as it was in the same air mass. Only radiosondes launched within a 2-hour window before or a 1-hour window hour after CI were included. To assess if a two-hour time window preceding CI is representative of the thermodynamic characteristics of the storm-inflow environment, we computed the average difference in potential temperature (θ) and mixing ratio (q_v) profiles between consecutive soundings (launched 1.5 hours apart) from fixed ARM sites, provided they were in the same airmass. We found that for the maritime airmass (sea or bay breeze), changes in θ and q_v remained within ± 1 K and ± 1 g kg^{-1} across all vertical levels (not shown). However, continental soundings exhibited greater θ deviations below 2 km AGL ($\sim$ 2 K change in the mean value), while q_v changes were confined to the ± 1 g kg^{-1} range. Limiting the time window to ± 1 hour around CI would likely yield θ and q_v changes about two-thirds of those mentioned above. However, the reduction in the sample size of unique paired soundings to cells, and consequent potential impact on the robustness of the statistical tests, outweighs the benefits of capturing a more precise environmental representation using a ± 1 hour time window.

We paired the environmental profile data for each category–transitioning cells (63 maritime and 41 continental) and shallow cells (302 maritime and 194 continental). However, since some cells shared the same radiosonde profile based on their initiation time and distance, we ensured independence among samples by performing significance tests only for the unique radiosonde profiles. For transitioning cells, the unique set of profiles reduced to 35 in the maritime regime and 21 in the continental regime. For shallow cells, we ended up with 32 and 66 unique profiles for continental and maritime regimes, respectively. Next, we employed the bootstrap hypothesis testing method (Dwivedi et al. 2017) to determine if the means of continental and maritime environmental variables were significantly different. The boxplot distributions of statistically significant environmental variables are presented in Fig. 14. When considering transitioning cells, we identified at least five variables (ML ECAPE, PBL depth, ML LCL, ML LFC, and diluted

EL) with significantly different means between maritime and continental air masses. Diluted EL is defined as the altitude where a lifted parcel loses its buoyancy and becomes cooler than the environmental temperature, factoring in the entrainment effect. The maritime air mass exhibited larger values for ML ECAPE and diluted EL, while continental air mass had higher values for the remaining boundary layer-related variables. For shallow cells, only TPW was found to be statistically significant, with larger average value in the maritime air mass.

Although there were significant differences in thermodynamic environments across the SBF, transitioning cells primarily differed in average cell area and to some extent in average composite reflectivity (Figs. 11f and b, respectively), while for shallow cells, the most pronounced distinction was observed in the average composite reflectivity (Fig. 11a). When viewed in conjunction with the results presented in Fig. 14, it appears that TPW was the most influential variable for differences in average composite reflectivity for shallow cells. However, we did not find an obvious functional form of a relationship between TPW and average cell reflectivity in shallow cells. Similarly, for transitioning cells, there was no obvious functional form that fit the average cell area and the significant environmental variables. However, these results suggest that environmental heterogeneity across the SBF played a role in favoring maritime cells to attain larger reflectivity in shallow cells and larger cell area and composite reflectivity in transitioning cells.

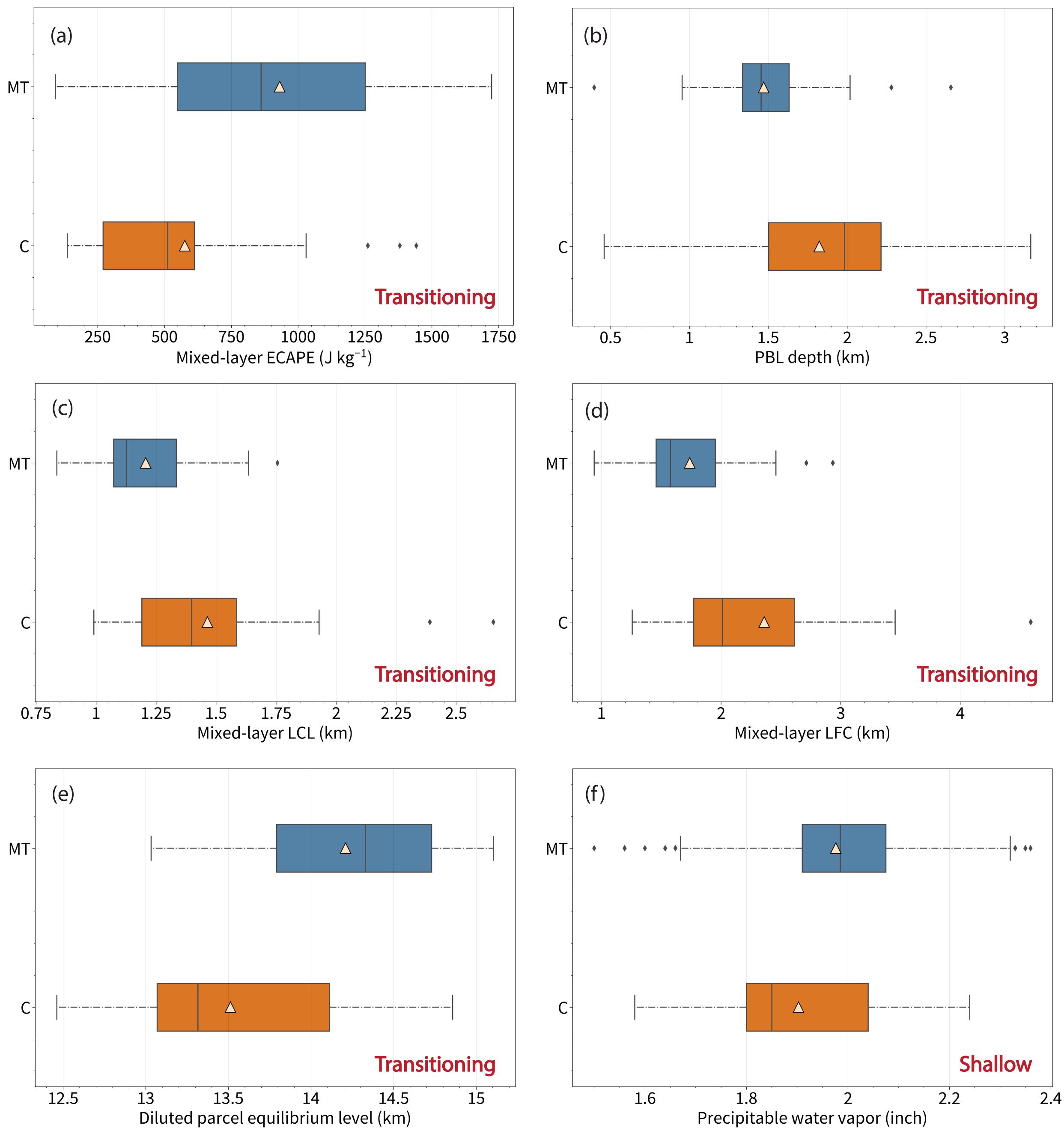

Fig. 14. Boxplot comparison of environmental variables with statistically significant difference in mean values between maritime (blue; MT) and continental (orange; C) air masses. Panels (a–e) correspond to variables that had significant differences for transitioning cells, and panel (f) for shallow cells. Mean and median values of each variable are indicated by a white triangle and a solid black line within each boxplot, respectively.

4. Summary and Discussion

This research was conducted during the DOE TRACER field campaign, aimed to improve our understanding of how meteorological and aerosol environments influence the evolution of deep convective clouds. The primary objective of this study was to quantify the spatiotemporal variability in thermodynamic and kinematic environments, and convective cell characteristics across sea- and bay-breeze fronts in the Houston, Texas region from June to September 2022. We analyzed a total of 177 radiosonde profiles collected at different locations and/or times, spanning over 15 different deployment days. We used these profiles to differentiate the mean composite vertical profiles of temperature and moisture during early and late afternoon hours and to establish representative environmental conditions for convection in both continental and maritime air masses.

Throughout the analysis period, we tracked more than 2300 unique cells from KHGX data, from which 501 shallow and 162 transitioning cells were selected to study the temporal evolution of composite reflectivity and maximum 20-dBZ echo-top height for convection that initiated within continental and maritime air masses or along the sea-breeze front. Furthermore, we identified a total of 49 isolated deep convective clouds from the CSAPR2 cell tracking database to compare the vertical profiles of Z_H, Z_{DR}, and K_{DP} in different air masses. Finally, to test how the environmental differences across air masses influences cell attributes, we subsampled the cell track dataset to select 63 maritime and 41 continental transitioning cells. The main findings from our analysis are:

(i) Convection associated with the inland propagation of the SBF typically peaked between 1400 and 1500 LT. Over 70% of the total tracked cells between 1100 and 1900 LT had a lifetime of 45 minutes or less. Specifically, shallow cells had a median lifetime of 24 minutes, while transitioning cells had a median lifetime of 49 minutes. Cells initiating between 1000 and 1200 LT demonstrated the maximum cell area and 20-dBZ echo-top height (Fig. 3). Two major CI hotspots were observed (Fig. 5): one located directly to the east of downtown Houston (and the AMF1 site) and the other southwest of Houston (directly above the ANC site).

(ii) The composite environmental profile for the TAMU site was found to be the driest in the upper boundary layer and lower free troposphere (950–700 hPa layer) in the early afternoon (maritime air mass) and mid-levels (600–400 hPa layer) in the late afternoon (continental air mass), respectively (Fig. 6). Additionally, a drier boundary layer in the late afternoon led to lower ML CAPE in the continental air mass.

(iii) The composite reflectivity of shallow and transitioning clouds followed a consistent temporal trend across air masses (Fig. 11a and b). Shallow clouds experienced the largest difference in mean composite reflectivity, with cells initiating close to SBF having the highest reflectivity values (41–44 dBZ), followed by maritime (36–40 dBZ) and continental (30–35 dBZ) cells. The distinction was less clear for transitioning cells, but still followed a similar pattern. The time series of mean composite 20-dBZ echo-top height exhibited significant overlap across air masses for both shallow and transitioning clouds (Fig. 11c and d).

(iv) Composite reflectivity of transitioning cells from CSAPR2 vertical profiles was found to be slightly larger than that from NEXRAD. Additionally, maritime cells in CSAPR2 data were qualitatively weaker, when comparing the reflectivity and differential reflectivity profiles (Fig. 12)

(v) Five environmental variables exhibited statistically significant differences in mean values between maritime and continental environments associated with transitioning cells. These variables include ML ECAPE, ML LCL, ML LFC, diluted EL, and PBL depth (Fig. 14). Among shallow cells, TPW was the sole environmental variable with a significant difference between maritime and continental air masses.

a. Implications:

Findings (iii) and (iv) suggest that variability in total moisture content between maritime and continental air masses may be the predominant meteorological factor influencing the bulk (warm rain) microphysical processes in shallow clouds. For transitioning cells, both lateral entrainment (and thus buoyancy dilution) and boundary layer thermodynamics (LCL/LFC height, PBL depth) may control the overall evolution of clouds. The additional complexity of mixed and ice-phase microphysical processes in transitioning cells, combined with coarse spatiotemporal resolution of NEXRAD data may have masked actual differences in composite reflectivity between maritime and continental air masses. However, the evolution of cell area of transitioning cells was notably different across the two air mass regimes. This finding is consistent with the analysis of Marquis et al. (2023) wherein the authors found circumstantial evidence of cell area being positively correlated with LCL height and boundary layer depth for CI in Argentina during the CACTI field campaign. This result also reaffirms that relying solely on CAPE as a predictor of deep convection behavior may not be sufficient (Zipser 2003; Sherwood et al. 2004; Robinson et al. 2008). High-resolution large-eddy simulations have highlighted that additional factors play crucial roles in the transition from shallow-to-deep convection (Morrison et al. 2022). Sub-cloud ascent, which represents overall thermodynamic forcing, along with environmental free-tropospheric humidity and dynamic entrainment, are also known to influence the likelihood of this transition. These factors should be taken into account when understanding the behavior of deep convective clouds.

The minimal contrast observed in mean 20-dBZ echo-top height values across different air masses and cloud types raises several possibilities. First, it suggests that the 20-dBZ echo-top height may not be the best proxy for determining convection intensity. Alternatively, it could indicate that transitioning cells were actually indistinguishable in intensity across different air masses. Another plausible explanation is that the coarse temporal resolution of KHGX radar was insufficient to resolve the variability in thunderstorm intensity acting at shorter time scales, as evident in CSAPR2 data (Fig. 13).

b. Caveats:

SBF cells exhibited the strongest shallow convection, and the longest track duration (not shown), which might be attributed to the reinforced updraft caused by surface convergence and cold pool-updraft interactions (Houston and Wilhelmson 2011), providing additional forcing for the parcel ascent to trigger deep convection. However, we avoided pairing the SBF cells with an environmental profile due to the uncertainty in determining which sounding, on either side of the SBF, most accurately represents the storm inflow along the convergence zone at the leading edge of the SBF.

The discrepancy between the air mass with maximum composite reflectivity values using CSAPR2 and KHGX data is likely due to small scale spatiotemporal perturbations in cloud micro-physical processes. These perturbations can be easily missed by slower KHGX updates or lost in the coarse PPI volume resolution. Additionally, the limited sample size of isolated deep convective cells by CSAPR2 is insufficient for generalizing our findings. Future efforts should focus on consistently collecting the full lifecycle of dual-pol radar variables in isolated deep convection across different air mass regimes to obtain statistically robust samples and identify potential differences in storm microphysical characteristics and evolution.

The identification of the parent mesoscale air mass for radiosonde launches and convective cell initiation involved some subjectivity. The data from weather radars, GOES-16 satellite, and surface meteorological stations sometimes failed to capture subtle changes in frontal boundary location or associated meteorological variables during sea-breeze front passage. Additionally, the sea breeze was often mixed with outflow from current or previous convective cells, as well as the bay breeze from the Galveston Bay region. Despite these challenges, we do not expect significant changes in the overall conclusions drawn from our results.

c. Conclusions and future efforts:

The main findings of this study support our initial hypothesis that maritime convection generally exhibits larger composite reflectivity (more pronounced in shallow cells and less so in transitioning cells) and wider cells (exclusively in transitioning cells) in comparison to continental convection. However, the relatively limited contrast in 20-dBZ echo-top height across different air masses and convection types serves as a reminder to exercise caution when assessing convective intensity based on radar-inferred echo-top heights. Nonetheless, many questions remain unanswered, including the mechanisms governing the responses of shallow and transitioning cells to the air mass heterogeneities, the extent to which radar reflectivity-based metrics capture microphysical evolution rather than updraft intensity, and the roles of secondary shallow circulations such as cold pools, differential radiative heating, and urban heat island circulations in promoting or suppressing convection within each air mass.

Additionally, our team's analysis of aerosol measurements has revealed substantial gradients in aerosol concentration and remarkable variability in aerosol size distribution across the air mass boundaries in the greater Houston region, as detailed in a companion paper. In future work, we plan to investigate the contribution of aerosols to microphysical differences observed in the shallow and transitioning cells and also the deeper Z_{DR} columns in continental cells indicated by CSAPR2. We intend to perform controlled idealized numerical experiments, considering both the observed spatial variability in thermodynamic environments and the vertical variability in aerosol concentration in order to understand the pathways involved in differential response of convection across various air mass regimes.

CRediT (Contributor Roles Taxonomy) statement. MS: Data curation, formal analysis, investigation, methodology, software, visualization, writing – original draft. ADR: Conceptualization, supervision, funding acquisition, project administration, resources, validation, writing – review and editing. CJN: Conceptualization, supervision, funding acquisition, resources, writing – review and editing. SDB: Conceptualization, funding acquisition.

Acknowledgments. We thank the U.S. Department of Energy (DOE)'s Atmospheric Radiation Measurement (ARM) data facility and the DOE TRACER field campaign. The authors acknowledge support by the DOE's Atmospheric System Research (ASR) grant DOE/SC-ARM-23-023. We also thank Drs. Erik Nielsen, Montana Etten-Bohm, and Don Conlee and the undergraduate students in the Department of Atmospheric Sciences at Texas A&M University for assisting with radiosonde instrumentation, data collection, and nowcasting efforts during TAMU TRACER. We appreciate Dr. Zhe Feng's assistance in debugging PyFLEXTRKR code, and Dr. John Peters for sharing his ECAPE code. We also extend our gratitude to Drs. Paul Walter and James Flynn for their hard work in collecting and sharing the TRACER-Sonde and TRACER-TCEQ-AQ2 radiosonde data. Finally, our heartfelt thanks to the creators and contributors of several open source Python software packages, especially PyART (Helmus and Collis 2016), NumPy (Harris et al. 2020), Dask (Dask Development Team 2016), SciPy (Virtanen et al. 2020), xarray (Hoyer and Hamman 2017), MetPy (May et al. 2008), and SHARPpy (Blumberg et al. 2017) which were used in this study. Data visualization for this study was performed using matplotlib (Hunter 2007) and ProPlot (Davis 2021).

Data availability statement. TAMU radiosonde data are available to download at `https://doi.org/10.5439/1968819`. ARM radiosonde data are available to download from the DOE ARM data repository (Keeler and Burk). TRACER-Sonde radiosonde data are available to download at `https://doi.org/10.5439/1996194`. TRACER-TCEQ-AQ2 data should be available to download from the NASA ASDC repository soon . Processed CSAPR2 scan bundle data used in this study are also available to download from the DOE ARM data repository (Oue et al. 2023). KHGX level-II data can be downloaded from the National Centers for Environmental Information (NCEI) NEXRAD data inventory (NOAA National Weather Service (NWS) Radar Operations Center 1991). PyFLEXTRKR software can be downloaded at `https://github.com/FlexTRKR/PyFLEXTRKR`. The processing code, including PyFLEXTRKR configuration files and jupyter notebooks used for analysis and plotting will be made available at 10.5281/zenodo.8414956 after the manuscript is accepted for publication.

References

Bachmann, K., C. Keil, G. C. Craig, M. Weissmann, and C. A. Welzbacher, 2020: Predictability of Deep Convection in Idealized and Operational Forecasts: Effects of Radar Data Assimilation, Orography, and Synoptic Weather Regime. *Monthly Weather Review*, **148 (1)**, 63–81, https://doi.org/10.1175/MWR-D-19-0045.1.

Bechtold, P., N. Semane, P. Lopez, J.-P. Chaboureau, A. Beljaars, and N. Bormann, 2014: Representing Equilibrium and Nonequilibrium Convection in Large-Scale Models. *Journal of the Atmospheric Sciences*, **71 (2)**, 734–753, https://doi.org/10.1175/JAS-D-13-0163.1.

Birch, C. E., M. J. Roberts, L. Garcia-Carreras, D. Ackerley, M. J. Reeder, A. P. Lock, and R. Schiemann, 2015: Sea-Breeze Dynamics and Convection Initiation: The Influence of Convective Parameterization in Weather and Climate Model Biases. *Journal of Climate*, **28 (20)**, 8093–8108, https://doi.org/10.1175/JCLI-D-14-00850.1.

Blumberg, W. G., K. T. Halbert, T. A. Supinie, P. T. Marsh, R. L. Thompson, and J. A. Hart, 2017: SHARPpy: An open-source sounding analysis toolkit for the atmospheric sciences. *Bulletin of the American Meteorological Society*, **98 (8)**, 1625–1636, https://doi.org/10.1175/BAMS-D-15-00309.1.

Böing, S. J., A. P. Siebesma, J. D. Korpershoek, and H. J. J. Jonker, 2012: Detrainment in deep convection. *Geophysical Research Letters*, **39 (20)**, https://doi.org/10.1029/2012GL053735.

Boubrahimi, S. F., B. Aydin, M. A. Schuh, D. Kempton, R. A. Angryk, and R. Ma, 2018: Spatiotemporal Interpolation Methods for Solar Event Trajectories. *ApJS*, **236 (1)**, 23, https://doi.org/10.3847/1538-4365/aab763.

Brast, M., R. A. J. Neggers, and T. Heus, 2016: What determines the fate of rising parcels in a heterogeneous environment? *Journal of Advances in Modeling Earth Systems*, **8 (4)**, 1674–1690, https://doi.org/10.1002/2016MS000750.

Bryan, G. H., J. C. Wyngaard, and J. M. Fritsch, 2003: Resolution Requirements for the Simulation of Deep Moist Convection. *Monthly Weather Review*, **131 (10)**, 2394–2416, https://doi.org/10.1175/1520-0493(2003)131⟨2394:RRFTSO⟩2.0.CO;2.

Chen, J., S. Hagos, Z. Feng, J. D. Fast, and H. Xiao, 2023: The Role of Cloud–Cloud Interactions in the Life Cycle of Shallow Cumulus Clouds. *Journal of the Atmospheric Sciences*, **80 (3)**, 671–686, https://doi.org/10.1175/JAS-D-22-0004.1.

Cheng, F.-Y., and D. W. Byun, 2008: Application of high resolution land use and land cover data for atmospheric modeling in the Houston–Galveston metropolitan area, Part I: Meteorological simulation results. *Atmospheric Environment*, **42 (33)**, 7795–7811, https://doi.org/10.1016/j.atmosenv.2008.04.055.

Colin, M., S. Sherwood, O. Geoffroy, S. Bony, and D. Fuchs, 2019: Identifying the Sources of Convective Memory in Cloud-Resolving Simulations. *Journal of the Atmospheric Sciences*, **76 (3)**, 947–962, https://doi.org/10.1175/JAS-D-18-0036.1.

Crosman, E. T., and J. D. Horel, 2010: Sea and Lake Breezes: A Review of Numerical Studies. *Boundary-Layer Meteorol*, **137 (1)**, 1–29, https://doi.org/10.1007/s10546-010-9517-9.

Dandou, A., M. Tombrou, and N. Soulakellis, 2009: The Influence of the City of Athens on the Evolution of the Sea-Breeze Front. *Boundary-Layer Meteorol*, **131 (1)**, 35–51, https://doi.org/10.1007/s10546-008-9306-x.

Dask Development Team, 2016: Dask: Library for dynamic task scheduling.

Davis, L. L. B., 2021: ProPlot. Zenodo, https://doi.org/10.5281/zenodo.5602155.

Dawe, J. T., and P. H. Austin, 2012: Statistical analysis of an LES shallow cumulus cloud ensemble using a cloud tracking algorithm. *Atmospheric Chemistry and Physics*, **12 (2)**, 1101–1119, https://doi.org/10.5194/acp-12-1101-2012.

Derbyshire, S. H., I. Beau, P. Bechtold, J.-Y. Grandpeix, J.-M. Piriou, J.-L. Redelsperger, and P. M. M. Soares, 2004: Sensitivity of moist convection to environmental humidity. *Quarterly Journal of the Royal Meteorological Society*, **130 (604)**, 3055–3079, https://doi.org/10.1256/qj.03.130.

Dwivedi, A. K., I. Mallawaarachchi, and L. A. Alvarado, 2017: Analysis of small sample size studies using nonparametric bootstrap test with pooled resampling method. *Statistics in Medicine*, **36 (14)**, 2187–2205, https://doi.org/10.1002/sim.7263.

Fast, J. D., and Coauthors, 2019: Overview of the HI-SCALE Field Campaign: A New Perspective on Shallow Convective Clouds. *Bulletin of the American Meteorological Society*, **100 (5)**, 821–840, https://doi.org/10.1175/BAMS-D-18-0030.1.

Feng, Z., J. Hardin, H. C. Barnes, J. Li, L. R. Leung, A. Varble, and Z. Zhang, 2023: PyFLEXTRKR: A flexible feature tracking Python software for convective cloud analysis. *Geoscientific Model Development*, **16 (10)**, 2753–2776, https://doi.org/10.5194/gmd-16-2753-2023.

Feng, Z., A. Varble, J. Hardin, J. Marquis, A. Hunzinger, Z. Zhang, and M. Thieman, 2022: Deep Convection Initiation, Growth, and Environments in the Complex Terrain of Central Argentina during CACTI. *Monthly Weather Review*, **150 (5)**, 1135–1155, https://doi.org/10.1175/MWR-D-21-0237.1.

Fovell, R. G., 2005: Convective Initiation ahead of the Sea-Breeze Front. *Monthly Weather Review*, **133 (1)**, 264–278, https://doi.org/10.1175/MWR-2852.1.

Fridlind, A. M., and Coauthors, 2019: Use of polarimetric radar measurements to constrain simulated convective cell evolution: A pilot study with Lagrangian tracking. *Atmospheric Measurement Techniques*, **12 (6)**, 2979–3000, https://doi.org/10.5194/amt-12-2979-2019.

Fu, S., R. Rotunno, J. Chen, X. Deng, and H. Xue, 2021: A large-eddy simulation study of deep-convection initiation through the collision of two sea-breeze fronts. *Atmospheric Chemistry and Physics*, **21 (12)**, 9289–9308, https://doi.org/10.5194/acp-21-9289-2021.

Fu, S., R. Rotunno, and H. Xue, 2022: Convective updrafts near sea-breeze fronts. *Atmospheric Chemistry and Physics*, **22 (11)**, 7727–7738, https://doi.org/10.5194/acp-22-7727-2022.

Genio, A. D. D., Y. Chen, D. Kim, and M.-S. Yao, 2012: The MJO Transition from Shallow to Deep Convection in CloudSat/CALIPSO Data and GISS GCM Simulations. *Journal of Climate*, **25 (11)**, 3755–3770, https://doi.org/10.1175/JCLI-D-11-00384.1.

Giangrande, S. E., T. S. Biscaro, and J. M. Peters, 2023: Seasonal controls on isolated convective storm drafts, precipitation intensity, and life cycle as observed during GoAmazon2014/5. *Atmospheric Chemistry and Physics*, **23 (9)**, 5297–5316, https://doi.org/10.5194/acp-23-5297-2023.

Grabowski, W. W., 2015: Untangling Microphysical Impacts on Deep Convection Applying a Novel Modeling Methodology. *Journal of the Atmospheric Sciences*, **72 (6)**, 2446–2464, https://doi.org/10.1175/JAS-D-14-0307.1.

Grabowski, W. W., and Coauthors, 2006: Daytime convective development over land: A model intercomparison based on LBA observations. *Quarterly Journal of the Royal Meteorological Society*, **132 (615)**, 317–344, https://doi.org/10.1256/qj.04.147.

Harris, C. R., and Coauthors, 2020: Array programming with NumPy. *Nature*, **585 (7825)**, 357–362, https://doi.org/10.1038/s41586-020-2649-2.

Harvey, N. J., C. L. Daleu, R. A. Stratton, R. S. Plant, S. J. Woolnough, and A. J. Stirling, 2022: The impact of surface heterogeneity on the diurnal cycle of deep convection. *Quarterly Journal of the Royal Meteorological Society*, **148 (749)**, 3509–3527, https://doi.org/10.1002/qj.4371.

Heikenfeld, M., B. White, L. Labbouz, and P. Stier, 2019: Aerosol effects on deep convection: The propagation of aerosol perturbations through convective cloud microphysics. *Atmospheric Chemistry and Physics*, **19 (4)**, 2601–2627, https://doi.org/10.5194/acp-19-2601-2019.

Helmus, J., and S. Collis, 2016: The Python ARM Radar Toolkit (Py-ART), a Library for Working with Weather Radar Data in the Python Programming Language. *Journal of Open Research Software*, **4 (1)**, e25, https://doi.org/10.5334/jors.119.

Henkes, A., G. Fisch, L. A. T. Machado, and J.-P. Chaboureau, 2021: Morning boundary layer conditions for shallow to deep convective cloud evolution during the dry season in the central Amazon. *Atmospheric Chemistry and Physics*, **21 (17)**, 13 207–13 225, https://doi.org/10.5194/acp-21-13207-2021.

Hohenegger, C., and B. Stevens, 2013: Preconditioning Deep Convection with Cumulus Congestus. *Journal of the Atmospheric Sciences*, **70 (2)**, 448–464, https://doi.org/10.1175/JAS-D-12-089.1.

Hopper, L. J., C. Schumacher, K. Humes, and A. Funk, 2020: Drop-Size Distribution Variations Associated with Different Storm Types in Southeast Texas. *Atmosphere*, **11 (1)**, 8, https://doi.org/10.3390/atmos11010008.

Houston, A. L., and R. B. Wilhelmson, 2011: The Dependence of Storm Longevity on the Pattern of Deep Convection Initiation in a Low-Shear Environment. *Monthly Weather Review*, **139 (10)**, 3125–3138, https://doi.org/10.1175/MWR-D-10-05036.1.

Hoyer, S., and J. Hamman, 2017: Xarray: N-D labeled arrays and datasets in Python. *Journal of Open Research Software*, **5 (1)**, https://doi.org/10.5334/jors.148.

Hunter, J. D., 2007: Matplotlib: A 2D graphics environment. *Computing in Science & Engineering*, **9 (3)**, 90–95, https://doi.org/10.1109/MCSE.2007.55.

Jensen, M. P., and Coauthors, 2016: The Midlatitude Continental Convective Clouds Experiment (MC3E). *Bulletin of the American Meteorological Society*, **97 (9)**, 1667–1686, https://doi.org/10.1175/BAMS-D-14-00228.1.

Jensen, M. P., and Coauthors, 2022: A Succession of Cloud, Precipitation, Aerosol, and Air Quality Field Experiments in the Coastal Urban Environment. *Bulletin of the American Meteorological Society*, **103 (2)**, 103–105, https://doi.org/10.1175/BAMS-D-21-0104.1.

Johnson, R. H., T. M. Rickenbach, S. A. Rutledge, P. E. Ciesielski, and W. H. Schubert, 1999: Trimodal Characteristics of Tropical Convection. *Journal of Climate*, **12 (8)**, 2397–2418, https://doi.org/10.1175/1520-0442(1999)012⟨2397:TCOTC⟩2.0.CO;2.

Keeler, E., and K. Burk, ????: Balloon-borne sounding system (SONDEWNPN). https://doi.org/10.5439/1595321.

Khain, A., D. Rosenfeld, and A. Pokrovsky, 2005: Aerosol impact on the dynamics and microphysics of deep convective clouds. *Quarterly Journal of the Royal Meteorological Society*, **131 (611)**, 2639–2663, https://doi.org/10.1256/qj.04.62.

Khairoutdinov, M., and D. Randall, 2006: High-Resolution Simulation of Shallow-to-Deep Convection Transition over Land. *Journal of the Atmospheric Sciences*, **63 (12)**, 3421–3436, https://doi.org/10.1175/JAS3810.1.

Kirshbaum, D. J., 2011: Cloud-Resolving Simulations of Deep Convection over a Heated Mountain. *Journal of the Atmospheric Sciences*, **68 (2)**, 361–378, https://doi.org/10.1175/2010JAS3642.1.

Kollias, P., E. Luke, M. Oue, and K. Lamer, 2020: Agile Adaptive Radar Sampling of Fast-Evolving Atmospheric Phenomena Guided by Satellite Imagery and Surface Cameras. *Geophysical Research Letters*, **47 (14)**, e2020GL088 440, https://doi.org/10.1029/2020GL088440.

Kurowski, M. J., K. Suselj, and W. W. Grabowski, 2019: Is Shallow Convection Sensitive to Environmental Heterogeneities? *Geophysical Research Letters*, **46 (3)**, 1785–1793, https://doi.org/10.1029/2018GL080847.

Lamer, K., P. Kollias, E. P. Luke, B. P. Treserras, M. Oue, and B. Dolan, 2023: Multisensor Agile Adaptive Sampling (MAAS): A methodology to collect radar observations of convective cell lifecycle. *Journal of Atmospheric and Oceanic Technology*, **-1 (aop)**, https://doi.org/10.1175/JTECH-D-23-0043.1.

Lebo, Z., 2018: A Numerical Investigation of the Potential Effects of Aerosol-Induced Warming and Updraft Width and Slope on Updraft Intensity in Deep Convective Clouds. *Journal of the Atmospheric Sciences*, **75 (2)**, 535–554, https://doi.org/10.1175/JAS-D-16-0368.1.

Li, Z., F. Niu, J. Fan, Y. Liu, D. Rosenfeld, and Y. Ding, 2011: Long-term impacts of aerosols on the vertical development of clouds and precipitation. *Nature Geosci*, **4 (12)**, 888–894, https://doi.org/10.1038/ngeo1313.

Lock, N. A., and A. L. Houston, 2014: Empirical examination of the factors regulating thunderstorm initiation. *Mon. Wea. Rev.*, **142 (1)**, 240–258, https://doi.org/10.1175/MWR-D-13-00082.1.

Marinescu, P. J., and Coauthors, 2021: Impacts of Varying Concentrations of Cloud Condensation Nuclei on Deep Convective Cloud Updrafts—A Multimodel Assessment. *Journal of the Atmospheric Sciences*, **78 (4)**, 1147–1172, https://doi.org/10.1175/JAS-D-20-0200.1.

Marquis, J. N., Z. Feng, A. Varble, T. C. Nelson, A. Houston, J. M. Peters, J. P. Mulholland, and J. Hardin, 2023: Near-cloud atmospheric ingredients for deep convection initiation. *Monthly Weather Review*, **-1 (aop)**, https://doi.org/10.1175/MWR-D-22-0243.1.

Martin, S. T., and Coauthors, 2017: The Green Ocean Amazon Experiment (GoAmazon2014/5) Observes Pollution Affecting Gases, Aerosols, Clouds, and Rainfall over the Rain Forest. *Bulletin of the American Meteorological Society*, **98 (5)**, 981–997, https://doi.org/10.1175/BAMS-D-15-00221.1.

Martin, W. J., and M. Xue, 2006: Sensitivity Analysis of Convection of the 24 May 2002 IHOP Case Using Very Large Ensembles. *Monthly Weather Review*, **134 (1)**, 192–207, https://doi.org/10.1175/MWR3061.1.

May, R. M., S. C. Arms, P. Marsh, E. Bruning, J. R. Leeman, K. Goebbert, J. E. Thielen, and Z. S. Bruick, 2008: MetPy: A Python Package for Meteorological Data. Boulder, Colorado, Unidata, https://doi.org/10.5065/D6WW7G29.

Morrison, H., and W. W. Grabowski, 2011: Cloud-system resolving model simulations of aerosol indirect effects on tropical deep convection and its thermodynamic environment. *Atmospheric Chemistry and Physics*, **11 (20)**, 10 503–10 523, https://doi.org/10.5194/acp-11-10503-2011.

Morrison, H., J. M. Peters, K. K. Chandrakar, and S. C. Sherwood, 2022: Influences of Environmental Relative Humidity and Horizontal Scale of Subcloud Ascent on Deep Convective Initiation. *Journal of the Atmospheric Sciences*, **79 (2)**, 337–359, https://doi.org/10.1175/JAS-D-21-0056.1.

Moser, D. H., and S. Lasher-Trapp, 2017: The Influence of Successive Thermals on Entrainment and Dilution in a Simulated Cumulus Congestus. *Journal of the Atmospheric Sciences*, **74 (2)**, 375–392, https://doi.org/10.1175/JAS-D-16-0144.1.

Nelson, T. C., J. Marquis, J. M. Peters, and K. Friedrich, 2022: Environmental controls on simulated deep moist convection initiation occurring during RELAMPAGO-CACTI. *Journal of the Atmospheric Sciences*, **-1 (aop)**, https://doi.org/10.1175/JAS-D-21-0226.1.

Nicholls, M. E., R. A. Pielke, and W. R. Cotton, 1991: A Two-Dimensional Numerical Investigation of the interaction between Sea Breezes and Deep Convection over the Florida Peninsula. *Monthly Weather Review*, **119 (2)**, 298–323, https://doi.org/10.1175/1520-0493(1991)119⟨0298:ATDNIO⟩2.0.CO;2.

NOAA National Weather Service (NWS) Radar Operations Center, 1991: NOAA Next Generation Radar (NEXRAD) Level 2 Base Data. [KHGX]. NOAA National Centers for Environmental Information, https://doi.org/10.7289/V5W9574V.

Ohashi, Y., and H. Kida, 2002: Local Circulations Developed in the Vicinity of Both Coastal and Inland Urban Areas: A Numerical Study with a Mesoscale Atmospheric Model. *Journal of*

Applied Meteorology and Climatology, **41 (1)**, 30–45, https://doi.org/10.1175/1520-0450(2002)041⟨0030:LCDITV⟩2.0.CO;2.

Oue, M., B. Puigdoménech-Treserras, E. Luke, and P. Kollias, 2023: CSAPR2 cell-tracking data collected during TRACER. https://doi.org/10.5439/1969992.

Peters, J. M., D. R. Chavas, C.-Y. Su, H. Morrison, and B. E. Coffer, 2023: An analytic formula for entraining CAPE in mid-latitude storm environments. *Journal of the Atmospheric Sciences*, **-1 (aop)**, https://doi.org/10.1175/JAS-D-23-0003.1.

Peters, J. M., H. Morrison, A. C. Varble, W. M. Hannah, and S. E. Giangrande, 2020: Thermal Chains and Entrainment in Cumulus Updrafts. Part II: Analysis of Idealized Simulations. *Journal of the Atmospheric Sciences*, **77 (11)**, 3661–3681, https://doi.org/10.1175/JAS-D-19-0244.1.

Rieck, M., C. Hohenegger, and C. C. van Heerwaarden, 2014: The Influence of Land Surface Heterogeneities on Cloud Size Development. *Monthly Weather Review*, **142 (10)**, 3830–3846, https://doi.org/10.1175/MWR-D-13-00354.1.

Robinson, F. J., S. C. Sherwood, and Y. Li, 2008: Resonant Response of Deep Convection to Surface Hot Spots. *Journal of the Atmospheric Sciences*, **65 (1)**, 276–286, https://doi.org/10.1175/2007JAS2398.1.

Romps, D. M., and Z. Kuang, 2010: Nature versus Nurture in Shallow Convection. *Journal of the Atmospheric Sciences*, **67 (5)**, 1655–1666, https://doi.org/10.1175/2009JAS3307.1.

Rousseau-Rizzi, R., D. J. Kirshbaum, and M. K. Yau, 2017: Initiation of Deep Convection over an Idealized Mesoscale Convergence Line. *Journal of the Atmospheric Sciences*, **74 (3)**, 835–853, https://doi.org/10.1175/JAS-D-16-0221.1.

Schlemmer, L., and C. Hohenegger, 2014: The Formation of Wider and Deeper Clouds as a Result of Cold-Pool Dynamics. *Journal of the Atmospheric Sciences*, **71 (8)**, 2842–2858, https://doi.org/10.1175/JAS-D-13-0170.1.

Schlemmer, L., C. Hohenegger, J. Schmidli, and C. Schär, 2012: Diurnal equilibrium convection and land surface–atmosphere interactions in an idealized cloud-resolving model. *Quarterly*

Journal of the Royal Meteorological Society, **138 (667)**, 1526–1539, https://doi.org/10.1002/qj.1892.

Sherwood, S. C., P. Minnis, and M. McGill, 2004: Deep convective cloud-top heights and their thermodynamic control during CRYSTAL-FACE. *Journal of Geophysical Research: Atmospheres*, **109 (D20)**, https://doi.org/10.1029/2004JD004811.

Steiner, M., R. A. Houze, and S. E. Yuter, 1995: Climatological Characterization of Three-Dimensional Storm Structure from Operational Radar and Rain Gauge Data. *Journal of Applied Meteorology and Climatology*, **34 (9)**, 1978–2007, https://doi.org/10.1175/1520-0450(1995)034⟨1978:CCOTDS⟩2.0.CO;2.

Suh, S.-H., H.-J. Kim, D.-I. Lee, and T.-H. Kim, 2021: Geographical Characteristics of Raindrop Size Distribution in the Southern Parts of South Korea. *Journal of Applied Meteorology and Climatology*, **60 (2)**, 157–169, https://doi.org/10.1175/JAMC-D-20-0102.1.

Thompson, R. L., C. M. Mead, and R. Edwards, 2007: Effective storm-relative helicity and bulk shear in supercell thunderstorm environments. *Wea. Forecasting*, **22 (1)**, 102–115, https://doi.org/10.1175/WAF969.1.

Thornton, J. A., K. S. Virts, R. H. Holzworth, and T. P. Mitchell, 2017: Lightning enhancement over major oceanic shipping lanes. *Geophysical Research Letters*, **44 (17)**, 9102–9111, https://doi.org/10.1002/2017GL074982.

Tian, Y., Y. Zhang, S. A. Klein, and C. Schumacher, 2021: Interpreting the Diurnal Cycle of Clouds and Precipitation in the ARM GoAmazon Observations: Shallow to Deep Convection Transition. *Journal of Geophysical Research: Atmospheres*, **126 (5)**, e2020JD033 766, https://doi.org/10.1029/2020JD033766.

Tuftedal, K. S., B. P. Treserras, M. Oue, and P. Kollias, 2023: Shallow and Deep Convection Characteristics in the Greater Houston, Texas Area Using Cell Tracking Methodology. *EGUsphere*, 1–46, https://doi.org/10.5194/egusphere-2023-821.

Varble, A. C., and Coauthors, 2021: Utilizing a Storm-Generating Hotspot to Study Convective Cloud Transitions: The CACTI Experiment. *Bulletin of the American Meteorological Society*, **102 (8)**, E1597–E1620, https://doi.org/10.1175/BAMS-D-20-0030.1.

Virtanen, P., and Coauthors, 2020: SciPy 1.0: Fundamental algorithms for scientific computing in python. *Nature Methods*, **17**, 261–272, https://doi.org/10.1038/s41592-019-0686-2.

Waite, M. L., and B. Khouider, 2010: The Deepening of Tropical Convection by Congestus Preconditioning. *Journal of the Atmospheric Sciences*, **67 (8)**, 2601–2615, https://doi.org/10.1175/2010JAS3357.1.

Wakimoto, R. M., and N. T. Atkins, 1994: Observations of the Sea-Breeze Front during CaPE. Part I: Single-Doppler, Satellite, and Cloud Photogrammetry Analysis. *Monthly Weather Review*, **122 (6)**, 1092–1114, https://doi.org/10.1175/1520-0493(1994)122⟨1092:OOTSBF⟩2.0.CO;2.

Walter, P., J. Flynn, Y. Wang, N. Partida, S. Yoon, R. Sheesley, and S. Usenko, 2023: TRACER-Sonde: O3 as a Tracer of Convective Mixing Field Campaign Report. Field Campaign Report DOE/SC-ARM-23-013, U.S. Department of Energy.

Weaver, C. P., 2004: Coupling between Large-Scale Atmospheric Processes and Mesoscale Land–Atmosphere Interactions in the U.S. Southern Great Plains during Summer. Part I: Case Studies. *Journal of Hydrometeorology*, **5 (6)**, 1223–1246, https://doi.org/10.1175/JHM-396.1.

Wilhelm, J., K. Wapler, U. Blahak, R. Potthast, and M. Kunz, 2023: Statistical relevance of meteorological ambient conditions and cell attributes for nowcasting the life cycle of convective storms. *Quart J Royal Meteoro Soc*, qj.4505, https://doi.org/10.1002/qj.4505.

Zhang, Y., and S. A. Klein, 2010: Mechanisms Affecting the Transition from Shallow to Deep Convection over Land: Inferences from Observations of the Diurnal Cycle Collected at the ARM Southern Great Plains Site. *Journal of the Atmospheric Sciences*, **67 (9)**, 2943–2959, https://doi.org/10.1175/2010JAS3366.1.

Zipser, E. J., 2003: Some Views On “Hot Towers” after 50 Years of Tropical Field Programs and Two Years of TRMM Data. *Meteorological Monographs*, **29 (51)**, 49–58, https://doi.org/10.1175/0065-9401(2003)029⟨0049:CSVOHT⟩2.0.CO;2.